Interstellar minor bodies in the Solar System

Dissertation for the degree of

doctor of philosophy

in Astronomy

by

Piotr Guzik

Supervisor: dr hab. Wacław Waniak
Auxiliary supervisor: dr Michał Drahus

Astronomical Observatory
Faculty of Physics, Astronomy and Applied Computer Science
Jagiellonian University

2023, Kraków

To my wife Ania and children Natalka, Tomek and Laura.

Acknowledgments

Abstract

The aim of this thesis is the characterization of interstellar minor bodies visiting the Solar System. Originating from protoplanetary disks around other stars, these objects undergo ejection into interstellar space due to planetary perturbations. When these samples of alien primordial matter pass through the Solar System, we may study them from very small distances with the well-known techniques of solar system science. That gives us unique direct insight into remote planetary systems. Though their visits have been expected for decades, they were started to be discovered only recently: the first one, 1I/'Oumuamua in 2017 and the second, 2I/Borisov in 2019.

This dissertation is a cycle of three publications focused on the photometric and spectroscopic characterization of these two objects: 1) the photometric study of 1I/'Oumuamua, 2) the report on initial imaging observations of 2I/Borisov taken immediately after its discovery, and 3) the spectroscopic study of 2I/Borisov, that led to the discovery of gaseous nickel in its coma.

The first publication presents photometric observations of 1I/'Oumuamua taken with the 8-m Gemini North telescope a few days after the discovery. Over two subsequent nights, we obtained more than 400 images with a total integration time of 3.58 hrs. The stacked image of 1I/'Oumuamua is the deepest ever taken and shows a completely stellar appearance. We then used the individual images to construct a precise lightcurve spanning over 8 hrs. The rotational lightcurve exhibited an enormous amplitude of 2.6 mag, larger than ever observed for any minor body native to the Solar System. Our result is consistent with a strongly elongated body, having an axis ratio of at least 5. The lightcurve indicated a rotation period of 7.56 hrs, however, minor inconsistencies between the cycles of rotation allowed us to discover that the body is tumbling, i.e. it is in a non-principal axis rotation state.

The second publication presents the earliest characterization of the second interstellar minor body, 2I/Borisov. Rapid reaction to this object was possible thanks to the dedicated

program which we developed after 1I/'Oumuamua. The program checks public databases containing astrometric measurements of newly discovered minor bodies in search of potential interstellar visitors and informs us if it detects a promising candidate. Our observations of 2I/Borisov using the 4-m William Herschel Telescope and the 8-m Gemini North telescope revealed that the second interstellar interloper is a familiar-looking comet with a nucleus radius of $\sim$1 km, and morphology, color, and dust properties typical to solar system comets.

In the third publication, we analyzed the UV part of the spectrum of 2I/Borisov, obtained with the X-Shooter spectrograph on the 8-m ESO/VLT telescope. The observations spanned three nights with an effective integration time of 3.84 hrs. The spectrum revealed emission lines of gaseous atomic nickel which has not been reported in any cold astrophysical environment before. The discovery was completely unexpected, since the comet was 2.32 astronomical units from the Sun at that time, with the temperature of its coma below 180 K and far below the melting point of nickel. We estimated the production rate of $0.9\pm0.3\times10^{22}$ atoms per second. We also analyzed the spatial profile of the detected lines and found out that nickel atoms originate from the parent molecule with a lifetime of 340^{+260}_{-200} seconds at 1 astronomical unit. All of the typical cometary emissions (i.e. CN, C_2, C_3, NH, NH_2, and OH) were also present in the spectrum, confirming the complete similarity of 2I/Borisov to solar system comets.

List of publications

This dissertation is prepared as a collection of the following, already published research papers:

1. Drahus, M., **Guzik, P.**, Waniak, W., Handzlik, B., Kurowski, S., Xu, S., Tumbling motion of 1I/'Oumuamua and its implications for the body's distant past, 2018, *Nature Astronomy*, 2, 407-412.

2. **Guzik, P.**, Drahus, M., Rusek, K., Waniak, W., Cannizzaro, G., Pastor-Marazuela, I., Initial characterization of interstellar comet 2I/Borisov, 2020, *Nature Astronomy*, 4, 53-57.

3. **Guzik, P.**, Drahus, M., Gaseous atomic nickel in the coma of interstellar comet 2I/Borisov, 2021, *Nature*, 593, 375-378.

Contents

1. Introduction

The Solar System contains comets and asteroids, collectively known as minor bodies. They consist of primitive material that was left after the formation of planets. Until recently, all known minor bodies were considered native to the Solar System but visitors from other planetary systems were also hypothesised for a long time. The first interstellar object, 1I/'Oumuamua, was discovered in 2017, followed by the detection of 2I/Borisov in 2019. These objects carry the matter that formed in other planetary systems and provide invaluable information about their birthplaces.

1.1 Solar system minor bodies

Comets have thrilled humans for millennia. Thanks to their sudden appearances and often spectacular look, they inspired both fear and fascination. Despite their ability to dominate the night sky, comets are actually small icy bodies known as cometary nuclei, composed mainly of water, carbon monoxide, and carbon dioxide mixed with dust. They are usually between hundreds of meters and a few dozen kilometers in size. When warmed by the Sun, they release gas and dust, forming a vast atmosphere called a coma, which can further interact with solar wind and radiation to create the iconic cometary tail.

On the other hand, asteroids are rocky objects that began to be discovered in the early 19th century. Their sizes range from a few meters to hundreds of kilometers. Unlike comets, these objects appeared completely stellar for many decades, when observed from the Earth, lacking any signs of gas or dust emissions.

Both comets and asteroids are remnants of the protoplanetary nebula from which our Solar System formed. Comets are believed to originate further away from the Sun, resulting in a higher content of volatiles, while rocky asteroids formed closer and do not contain significant amounts of ice. Many comets were scattered to the Oort Cloud, a spherical structure in the outer regions of the Solar System, while most asteroids remained in the asteroid belt located between the orbits of Mars and Jupiter.

This simplified distinction between comets and asteroids has been recently challenged

with the discovery of new populations of minor bodies, such as active asteroids (Jewitt, 2012), main belt comets (Hsieh & Jewitt, 2006), or barely active objects coming from Oort Cloud (Meech et al., 2016).

1.2 Decades of expectations

Models of the early Solar System suggest that most minor bodies remaining after the formation of planets were ejected into interstellar space due to planetary perturbations (Dones et al., 2004). Considering the prevalence of planetary systems throughout the Galaxy, it can be inferred that the entire Galaxy is likely filled with remnants from the formation of planetary systems - minor bodies traversing interstellar space, with occasional visits to the inner Solar System. These expectations have been postulated for several decades (Sekanina, 1976; McGlynn & Chapman, 1989; Cook et al., 2016). The prospect of directly detecting interstellar visitors gained momentum with the advancement of all-sky surveys, and on October 19, 2017, the first such object, 1I/'Oumuamua, was discovered (Meech et al., 2017).

1.3 1I/'Oumuamua

1I/'Oumuamua was first spotted by the PAN-STARRS survey a few weeks after its perihelion passage and during its closest approach to Earth (at the time of discovery, it was approximately 0.22 AU from Earth). Already early observations showed its extrasolar origin as its orbit displayed the eccentricity of 1.20 equivalent to hyperbolic excess velocity (the velocity relative to the Solar System when it was effectively at an infinite distance) of about 26 km/s.

Despite favorable geometric conditions, its brightness had never exceeded 19 mag, thus the study on this object was strictly limited to the largest telescopes. Although 1I/'Oumuamua appeared asteroidal, it was initially classified as a comet due to the prevailing notion that most interstellar minor bodies should be comets (e.g. Cook et al., 2016). This expectation stems from the fact that comets are formed further away from their home stars compared to asteroids, making their orbits less gravitationally bound and more susceptible to ejection into interstellar space.

The object quickly receded from both Earth and the Sun, rapidly fading, which limited the time available for its study. Initial deep images confirmed its completely stellar appearance and asteroidal nature (Drahus et al., 2018; Meech et al., 2017). The rotational lightcurve of 1I/'Oumuamua exhibited an enormous amplitude of 2.6 mag (Drahus et al.,

2018), the largest ever observed among minor bodies in the Solar System, indicating a highly irregular shape. Though the elongation ratios as large as 10:1 were postulated (Meech et al., 2017), the detailed lightcurve modeling indicates that the actual axis ratio needed to account for such large brightness variations may be as low as 5 (Drahus et al., 2018), with an effective radius of approximately 75 m. The reported rotational periods of the object seemed to be slightly inconsistent, varying between 7 and 8 hours, probably because of non-principal axis rotation of the object (Drahus et al., 2018; Fraser et al., 2018; Belton et al., 2018). Spectra taken during that time revealed a featureless profile with a moderately reddish slope, consistent with icy solar system minor bodies (Fitzsimmons et al., 2018).

Exceptional extrasolar origin of the object sparked the debate about the location of its birth. At first, it was noted that the motion of the object (i.e. both its direction and velocity) was nearly the same as that of the local standard rest (Mamajek, 2017) and did not fit the motion of any nearby star. Further, a much deeper search for its home planetary system (e.g. Dybczyński & Królikowska, 2018; Bailer-Jones et al., 2018) also failed to point it with certainty.

The peculiarities of the object combined with its extrasolar origin have given rise to speculations about its artificial origin which led to the search for radio emissions (Harp et al., 2019) with the world's premiere single dish radio telescope - 110-m Green Bank Telescope. No signal was detected, however.

The most unexpected discovery regarding 1I/'Oumuamua was reported a few months later. Archival astrometric data analysis revealed that the object deviated slightly from its gravitational path, apparently under the influence of unknown non-gravitational forces (Micheli et al., 2018). Such forces are present in the case of solar system minor bodies, but they are observed only in active comets. However, no trace of cometary activity from 1I/'Oumuamua has ever been detected. Despite this, the team that made the discovery favored sublimation as the most plausible source of the drag experienced by the object. To remain undetectable, the material released from the surface of 1I/'Oumuamua would need to consist of exceptionally large particles. This hypothesis has later been challenged by the considerations of rotational stability of the object (Guzik & Drahus, 2018; Rafikov, 2018). The non-gravitational forces were also consistent with the solar radiation pressure but that would require an exotic structure of the object (Moro-Martín, 2019) or even its artificial origin (Bialy & Loeb, 2018). New hypotheses trying to explain the oddities of 1I/'Oumuamua are constantly being developed (see e.g. Seligman & Laughlin, 2020; Jackson & Desch, 2021; Bergner & Seligman, 2023), but it is unlikely that any of them will ever be proven.

The only way to verify the mysterious nature of 1I/'Oumuamua would be through a space mission to this enigmatic object and indeed, such a mission has been proposed (Hein et al., 2019) with further modifications added later (Hibberd et al., 2020; Hibberd & Hein, 2021; Hibberd et al., 2022), though it will not be feasible with the current technology. On the other hand, another mission inspired by the visit of 1I/'Oumuamua, called "Comet Interceptor" (Jones & Snodgrass, 2019) has been selected by ESA and is being developed for launch in 2029 and is designed to approach either a pristine comet coming from the Oort cloud or another interstellar minor body if such an object with favorable trajectory is found.

1.4   2I/Borisov

Less than two years after the discovery of 1I/'Oumuamua, on August 30, 2019, the second interstellar visitor to the Solar System was identified. Contrary to expectations, this object, named 2I/Borisov, was surprisingly bright and was first spotted by an amateur astronomer named Gennadiy Borisov. It had gone unnoticed by automated all-sky surveys primarily due to its small solar elongation, which persisted for a significant period leading up to its discovery. The object's brightness was even more remarkable considering it was still well before perihelion, and it was expected to reach a magnitude of 15.

Initial observations of 2I/Borisov revealed a comet with a familiar appearance, displaying typical colors and morphology (Guzik et al., 2020). The radius of the cometary nucleus was initially estimated to be about 1 km, but later the observations made with Hubble Space Telescope refined this value to be between 0.2 km and 0.5 km (Jewitt et al., 2020a).

As observing conditions improved over time, the comet received extensive attention in the following months. Spectroscopic observations showed well-known emissions that indicated that the chemical composition of 2I/Borisov matches that of solar system comets. The first molecule detected was CN (Fitzsimmons et al., 2019; Kareta et al., 2020; de León et al., 2020), followed by C_2 (Lin et al., 2020), OI (McKay et al., 2020), NH_2 (Bannister et al., 2020), OH (Xing et al., 2020) and CO (Cordiner et al., 2020; Bodewits et al., 2020). Even the amount of the unexpected vapors of nickel found in its coma (Guzik & Drahus, 2021) turned out consistent with the simultaneously discovered metal vapors in comae of comets native to Solar System (Manfroid et al., 2021).

Following the discovery, the comet brightened according to expectations and its brightness reached 15 mag at the end of 2019, shortly after the perihelion passage. Then it started to fade, but at the beginning of March 2020, it experienced multiple outbursts which increased its brightness by about 0.7 mag (Drahus et al., 2020). Later, the observations

made with Hubble Space Telescope showed that the outburst was associated with the splitting of the comet's nucleus (Jewitt et al., 2020b).

Despite the fact that precise astrometry for 2I/Borisov covers a period longer than a year, including pre-discovery detection (Ye et al., 2020) when it was still more than 7 astronomical units from the Sun, its home planetary system cannot be established (Dybczyński et al., 2019; Bailer-Jones et al., 2020).

2. Motivation

Minor bodies are known to be the remnants of planetary formation. They are time capsules that preserve the primordial matter that once formed planets. Until very recently all of the known minor bodies were native to the Solar System, allowing us to study the distant past of our home.

Now, with the discovery of 1I/'Oumuamua followed by 2I/Borisov, a new era of planetary science has begun. Each interstellar interloper is in fact a sample of extra-solar matter, representing primordial matter that was left after the formation of an alien planetary system. Thus, while studying interstellar minor bodies traversing the Solar System, we study other planetary systems from up close without the need for interstellar travel. We can inspect their physical properties as well as their chemical composition with well-established methods and techniques used to study our native comets and asteroids.

The main objective of my research conducted while preparing the doctoral dissertation is to understand these new objects in the Solar System that have never been observed before. What are they and what do they look like? What are they made of? How similar are they to "our" comets and asteroids, and how do they differ from each other? Do the places they come from resemble our Solar System? Such questions arise from our innate curiosity about the world when something entirely new appears in our surroundings. In order to find answers to these questions, I strive to determine the basic characteristics of these distant visitors: their shape, size, color, density, chemical composition, and how they evolve under the influence of the energy they receive from the Sun. These studies are of fundamental importance for gaining a better understanding of extrasolar planetary systems and, consequently, our own Solar System in the broader context of our galaxy.

3. The future prospects

With the exciting advancements in all-sky surveys, particularly the start of operation of Vera C. Rubin Observatory in 2024, the imminent detection of next interstellar visitors seems to be inevitable. Indeed, the first estimates after the discovery of 1I/'Oumuamua indicated, that up to 10 000 such objects are present all the time within the orbit of Neptune (Jewitt et al., 2017) and they are not observed only because they do not reflect enough light to be within the range of the surveys at that time. The statistics inferred from the discovery led to suggestions that with the present surveys a new interstellar object should be discovered every few years (Jewitt et al., 2017; Do et al., 2018). Given that Vera C. Rubin observatory will reach roughly 10 times deeper then PAN-STARRS survey that was used to discover 1I/'Oumuamua, one may expect that up to a few interstellar interlopers will be discovered every year after the start of its operation. The most up-to-date statistical study (Flekkøy & Toussaint, 2023) argues that the discovery rate will not be that high, however it still indicates that with 66% probability the next 'Oumuamua-like object will be detected by Vera C. Rubin Observatory within a year and a half of its launch.

Bibliography

Bailer-Jones, C. A. L., Farnocchia, D., Meech, K. J., et al. 2018, AJ, 156, 205

Bailer-Jones, C. A. L., Farnocchia, D., Ye, Q., Meech, K. J., & Micheli, M. 2020, A&A, 634, A14

Bannister, M. T., Opitom, C., Fitzsimmons, A., et al. 2020, Interstellar comet 2I/Borisov as seen by MUSE: C_2, NH_2 and red CN detections. https://arxiv.org/abs/2001.11605

Belton, M. J. S., Hainaut, O. R., Meech, K. J., et al. 2018, ApJL, 856, L21

Bergner, J. B., & Seligman, D. Z. 2023, Nature, 615, 610

Bialy, S., & Loeb, A. 2018, ApJL, 868, L1

Bodewits, D., Noonan, J. W., Feldman, P. D., et al. 2020, Nature Astronomy, 4, 867

Cook, N. V., Ragozzine, D., Granvik, M., & Stephens, D. C. 2016, ApJ, 825, 51

Cordiner, M. A., Milam, S. N., Biver, N., et al. 2020, Nature Astronomy, 4, 861

de León, J., Licandro, J., de la Fuente Marcos, C., et al. 2020, MNRAS, 495, 2053

Do, A., Tucker, M. A., & Tonry, J. 2018, ApJL, 855, L10

Dones, L., Weissman, P. R., Levison, H. F., & Duncan, M. J. 2004, in Comets II, ed. M. C. Festou, H. U. Keller, & H. A. Weaver, 153

Drahus, M., Guzik, P., Waniak, W., et al. 2018, Nature Astronomy, 2, 407

Drahus, M., Guzik, P., Udalski, A., et al. 2020, The Astronomer's Telegram, 13549, 1

Dybczyński, P. A., & Królikowska, M. 2018, A&A, 610, L11

Dybczyński, P. A., Królikowska, M., & Wysoczańska, R. 2019, arXiv e-prints, arXiv:1909.10952

Fitzsimmons, A., Snodgrass, C., Rozitis, B., et al. 2018, Nature Astronomy, 2, 133

Fitzsimmons, A., Hainaut, O., Meech, K. J., et al. 2019, ApJL, 885, L9

Flekkøy, E. G., & Toussaint, R. 2023, MNRAS, 523, L9

Fraser, W. C., Pravec, P., Fitzsimmons, A., et al. 2018, Nature Astronomy, 2, 383

Guzik, P., & Drahus, M. 2018, in AAS/Division for Planetary Sciences Meeting Abstracts, Vol. 50, AAS/Division for Planetary Sciences Meeting Abstracts #50, 301.05

Guzik, P., & Drahus, M. 2021, Nature, 593, 375

Guzik, P., Drahus, M., Rusek, K., et al. 2020, Nature Astronomy, 4, 53

Harp, G. R., Richards, J., Jenniskens, P., Shostak, S., & Tarter, J. C. 2019, Acta Astronautica, 155, 51

Hein, A. M., Perakis, N., Eubanks, T. M., et al. 2019, Acta Astronautica, 161, 552

Hibberd, A., & Hein, A. M. 2021, Acta Astronautica, 179, 594

Hibberd, A., Hein, A. M., & Eubanks, T. M. 2020, Acta Astronautica, 170, 136

Hibberd, A., Hein, A. M., Eubanks, T. M., & Kennedy, R. G. 2022, Acta Astronautica, 199, 161

Hsieh, H. H., & Jewitt, D. 2006, Science, 312, 561

Jackson, A. P., & Desch, S. J. 2021, Journal of Geophysical Research (Planets), 126, e06706

Jewitt, D. 2012, AJ, 143, 66

Jewitt, D., Hui, M.-T., Kim, Y., et al. 2020a, ApJL, 888, L23

Jewitt, D., Kim, Y., Mutchler, M., et al. 2020b, ApJL, 896, L39

Jewitt, D., Luu, J., Rajagopal, J., et al. 2017, ApJL, 850, L36

Jones, G., & Snodgrass, C. 2019, in EGU General Assembly Conference Abstracts, EGU General Assembly Conference Abstracts, 15361

Kareta, T., Andrews, J., Noonan, J. W., et al. 2020, ApJL, 889, L38

Lin, H. W., Lee, C.-H., Gerdes, D. W., et al. 2020, ApJL, 889, L30

Mamajek, E. 2017, Research Notes of the American Astronomical Society, 1, 21

Manfroid, J., Hutsemékers, D., & Jehin, E. 2021, Nature, 593, 372

McGlynn, T. A., & Chapman, R. D. 1989, ApJL, 346, L105

McKay, A. J., Cochran, A. L., Dello Russo, N., & DiSanti, M. A. 2020, ApJL, 889, L10

Meech, K. J., Yang, B., Kleyna, J., et al. 2016, Science Advances, 2, e1600038

Meech, K. J., Weryk, R., Micheli, M., et al. 2017, Nature, 552, 378

Micheli, M., Farnocchia, D., Meech, K. J., et al. 2018, Nature, 559, 223

Moro-Martín, A. 2019, ApJL, 872, L32

Rafikov, R. R. 2018, ApJL, 867, L17

Sekanina, Z. 1976, Icarus, 27, 123

Seligman, D., & Laughlin, G. 2020, ApJL, 896, L8

Xing, Z., Bodewits, D., Noonan, J., & Bannister, M. T. 2020, ApJL, 893, L48

Ye, Q., Kelley, M. S. P., Bolin, B. T., et al. 2020, AJ, 159, 77

4. Publications

Tumbling motion of 1I/'Oumuamua and its implications for the body's distant past

Michał Drahus[1]*, Piotr Guzik[1]*, Wacław Waniak[1], Barbara Handzlik[1], Sebastian Kurowski[1] and Siyi Xu[2]

Models of the Solar System's evolution show that almost all the primitive material leftover from the formation of the planets was ejected to the interstellar space as a result of dynamical instabilities[1]. Accordingly, minor bodies should also be ejected from other planetary systems and should be abundant in the interstellar space[2], giving hope for their direct detection and detailed characterization as they penetrate through the Solar System[3,4]. These expectations materialized on 19 October 2017 UT with the Panoramic Survey Telescope and Rapid Response System's discovery of 1I/'Oumuamua[5]. Here, we report homogeneous photometric observations of this body from Gemini North, which densely cover a total of 8.06 h over two nights. A combined ultra-deep image of 1I/'Oumuamua shows no signs of cometary activity, confirming the results from other, less sensitive searches[6–9]. Our data also show an enormous range of rotational brightness variations of 2.6 ± 0.2 mag, larger than ever observed in the population of small Solar System objects, suggesting a very elongated shape of the body. Most significantly, the light curve does not repeat exactly from one rotation cycle to another and its double-peaked periodicity of 7.56 ± 0.01 h from our data is inconsistent with earlier determinations[6,7,10–12]. These are clear signs of a tumbling motion, a remarkable characteristic of 1I/'Oumuamua's rotation that is consistent with a collision in the distant past. Bearing marks of a violent history, this first-known interstellar visitor tells us that collisional evolution of minor body populations in other planetary systems might be common.

1I/'Oumuamua entered the Solar System from the direction of the solar apex with a large hyperbolic excess speed of 26 km s^{-1}, then reached perihelion at 0.26 au from the Sun on 9 September 2017 UT, approached the Earth to 0.16 au on 16 October 2017 UT and is currently on its way back to the interstellar space. Previous studies have not detected any signs of cometary activity[6–9] and reported an average V-band absolute magnitude of 22.4 to 22.95 (refs [6,7,9]). Such an intrinsically faint object could be discovered only thanks to the close Earth flyby in October 2017, which created a tremendous opportunity for the first detailed characterization of a minor body of exosolar origin. We were awarded director's discretionary time on the 8.1 m Gemini North telescope (programme GN-2017B-DD-7) to characterize this unique object photometrically using the Gemini Multi-Object Spectrograph (GMOS-N). On 27 and 28 October 2017 UT, we obtained a total of 431 r'-band[13] images suitable for accurate time-resolved photometry, having an effective integration time of 3.58 h and spanning a total of 8.06 h (see Methods). The images, among other reduction and calibration steps, were cleaned of background stars and galaxies interfering with 1I/'Oumuamua,

which resulted in an uncontaminated representation of the target on a very clean and uniform background (see Methods). Photometric measurements were made in the standard way (see Methods) and were geometrically corrected (brightness and time) to the standard epoch of the observations, 28 October 2017 at 00:00 UT.

In Fig. 1, we show a mean combined image of 1I/'Oumuamua. No signs of cometary activity can be seen, consistent with earlier reports[6–9]; however, the sensitivity of our image is a factor of two to ten higher than those achieved by the previous searches. The median flux corresponds to an apparent r'-band magnitude of 22.45 and an absolute magnitude of 22.1 (see Methods), the absolute magnitude being broadly consistent with those reported before[6,7,9]. More interestingly, the range of brightness variations is enormous—a factor of 11 ± 2, or 2.6 ± 0.2 mag (see Methods), and possibly more—which exceeds even the largest rotational variations observed in the population of Solar System asteroids. The photometric time series of 1I/'Oumuamua was scrutinized for periodicity using the classical phase dispersion minimization (PDM) algorithm[14] with implemented inverse-variance weighting of the data points[15] (see Methods). We found the best periodicity solution for a frequency of 0.13230 ± 0.00014 h^{-1}, or a 7.56 ± 0.01 h period (Fig. 2a), implying a double-peaked phased light curve (Fig. 2b) most easily explained by shape-dominated brightness variations. Although not as good, a corresponding single-peaked phasing, consistent with albedo-dominated brightness variations, is also clearly indicated by the periodograms at approximately twice the double-peaked frequency, 0.26584 ± 0.00011 h^{-1}, or half the double-peaked period, 3.762 ± 0.002 h (Supplementary Fig. 1). Other periodicities offer implausible data phasings and can be safely excluded (Supplementary Figs. 2–8). The reported temporal colour variations[11,16,17] of 1I/'Oumuamua could, in principle, provide additional constraints on the light curve periodicity. Unfortunately, the available colour information is too incomplete to be useful in this regard and thus is indifferent to the two above periodicity solutions. We proceed assuming shape-dominated brightness variations and, consequently, adopt the double-peaked periodicity as 1I/'Oumuamua's synodic rotation period. In terms of the rotation period, our target compares well to the population of Solar System asteroids. However, the period appears remarkably long if we restrict our comparison to the objects smaller than 200 m in diameter—a category that 1I/'Oumuamua probably falls into (see next paragraph)—dominated by rapidly rotating monoliths with non-negligible tensile strength[18]. In Fig. 3, we show the range of rotational variation and rotation period of 1I/'Oumuamua in the context of 16,213 Solar System asteroids with reliably measured light curves[19].

[1]Astronomical Observatory, Jagiellonian University, Kraków, Poland. [2]Gemini Observatory, Hilo, HI, USA. These authors contributed equally: M. Drahus and P. Guzik. *e-mail: drahus@oa.uj.edu.pl; piotr.guzik@doctoral.uj.edu.pl
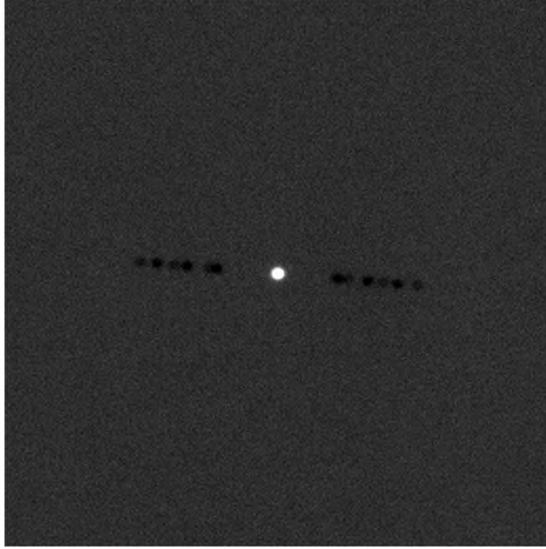
Fig. 1 | Deep stack of the r′-band imaging time series of 1I/'Oumuamua. The negative images of the target to the left and right of the positive image were produced using our background subtraction algorithm and do not affect the photometry. The presented region is 1.0 × 1.0 arcmin. North is to the top and east is to the left. Despite having a very high surface brightness sensitivity of 28.2 mag arcsec⁻² measured in a 1 arcsec² region, the image does not show any signs of cometary activity.

Using Hapke's reflectance model[20], we found from our data the spin-axis orientation to be within 25° from perpendicular to the line of sight, the long-to-short axis ratio to be >4.9 (see Fig. 4) and, assuming the rotation axis strictly perpendicular to the line of sight, we determined the volume-equivalent radius to be in the range 75–79 m (see Methods). Note that the axis ratio, though certainly very large, can still be much smaller than the measured range of brightness variations, in contrast with several previous reports[6,7,11] (see Methods). The very large elongation, together with the measured moderate rotation rate, require a density of >1,100 kg m⁻³ to prevent the body from falling apart (see Methods). This limit is calculated under the assumption that the tensile strength is negligible, which may or may not be true for 1I/'Oumuamua. Nonetheless, our estimate shows that the body may be strengthless and still have a density within the ranges of typical Solar System asteroids[21], again in contrast with most of the previous revelations[6,7,11] (see Methods).

While the light curve of 1I/'Oumuamua is clearly periodic, it does not repeat exactly from one rotation cycle to another. As we cannot explain this behaviour by instrumental effects, we conclude that it is a real feature of the light curve, intrinsic to the object. Furthermore, the light curve does not appear to have a single, unique periodicity because the rotation periods reported by other studies[6,7,10–12] differ from one another and are inconsistent with our data (Supplementary Figs. 9–12). We recognize these peculiarities as the characteristic signatures of non-principal-axis (or excited) rotation, also often referred to as tumbling[22,23], which has significant consequences for understanding the distant history of this object.

Although the vast majority of Solar System minor bodies do not show any measurable deviations from simple rotation, a small fraction of asteroids[19,22] and a few comets[24,25] have been identified as tumblers. In particular, comet 1P/Halley was the first minor body found in a non-principal-axis rotation state[24] and, subsequently, asteroid
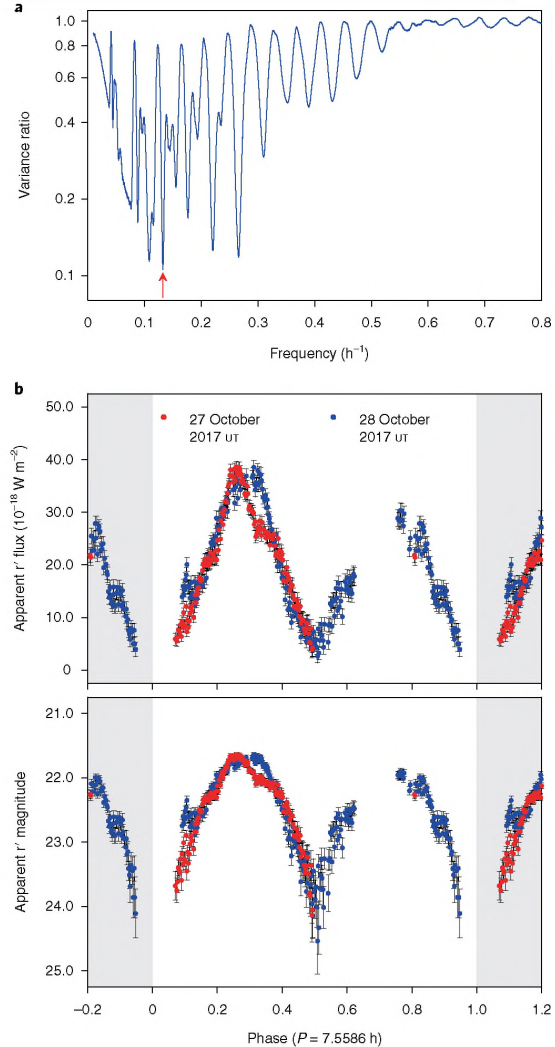

Fig. 2 | Results from the periodicity analysis of the r′-band photometric time series of 1I/'Oumuamua. a, Example of a weighted PDM periodogram[14,15], calculated for the time series expressed in flux using 20 bins and 5 covers (see Methods). The red arrow indicates the best periodicity solution for a frequency of 0.13230 ± 0.00014 h⁻¹, or a 7.56 ± 0.01 h period. **b,** Light curve phased using the best periodicity solution. The phase zero-point was chosen arbitrarily and corresponds to phase 0.979435 at the standard epoch of the observations, 28 October 2017 at 00:00 UT. The grey areas indicate replicated data. It is evident that the light curve does not repeat exactly from one night (27 October 2017 UT) to another (28 October 2017 UT), consistent with a non-principal-axis rotation state, or tumbling.

(4179) Toutatis was identified as the first tumbler among asteroids[26]. Rotational excitation occurs mainly through collisions and, restricted to comets, sublimation torques, but tidal and Yarkovsky-O'Keefe-Radzievskii-Paddack torques can also play an important role[27]. A tumbler then dissipates rotational energy due to stresses and strains resulting from complex rotation, and returns to a simple,
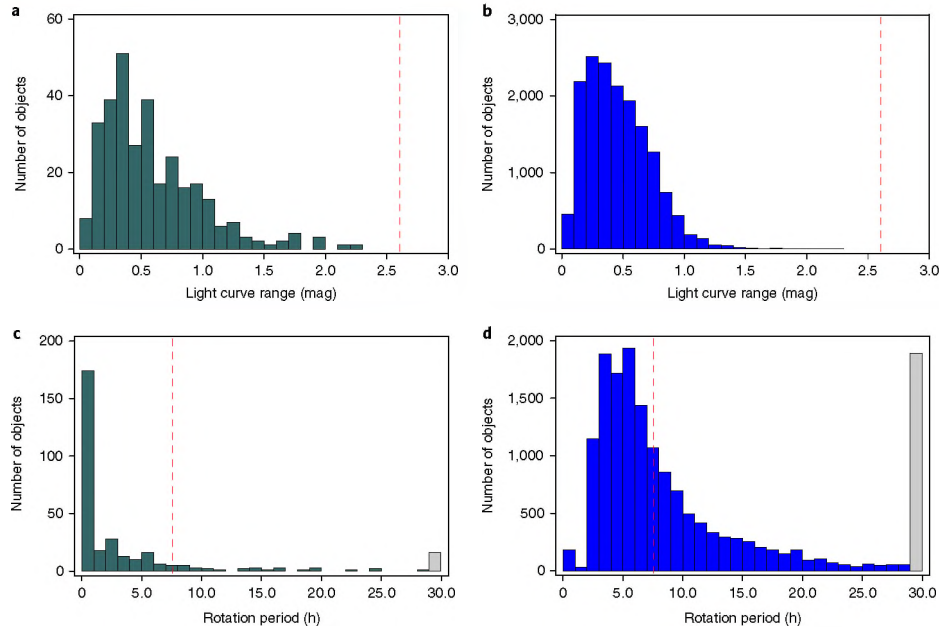
Fig. 3 | Light curve parameters of 1I/'Oumuamua in the context of 16,213 Solar System asteroids. Reference asteroid data (histograms) were taken from the minor planet Lightcurve Database[19] retrieved on 13 November 2017. The characteristics of our target (red dashed line) are compared separately against small asteroids with diameters <200 m (green), dominated by monoliths with non-negligible tensile strength[18], and against all objects (blue). Out-of-range values, where present, were added to the last bins (grey). **a**, Light curve ranges of 1I/'Oumuamua and small asteroids. **b**, Light curve ranges of 1I/'Oumuamua and all asteroids. **c**, Rotation periods of 1I/'Oumuamua and small asteroids. **d**, Rotation periods of 1I/'Oumuamua and all asteroids.

minimum-energy rotation state on a certain timescale. The damping (or relaxation) timescale depends on the object's size, shape, density, stiffness and rotation rate, and ranges from hundreds of years to hundreds of billions of years for the known Solar System asteroids[28]. Detailed quantification of 1I/'Oumuamua's complex rotation state is beyond the scope of this paper. Instead, we explore the fundamental fact that the body was once excited and has not fully relaxed to date.

Evidently, the rotational excitation of 1I/'Oumuamua is not easily explainable by sublimation torques. First, the object does not show any signs of active outgassing despite the superb sensitivity of our combined image (Fig. 1) and exceptionally favourable orbital circumstances. Second, it is unlikely that the body was active in the past because the sublimation levels required to excite its rotation would also generate enormous changes in the rotation rate, quickly leading to rotational instability and disruption. Instead, the complex rotation state of 1I/'Oumuamua may result from tidal or Yarkovsky–O'Keefe–Radzievskii–Paddack torques, but is most easily attributable to an impact—our preferred explanation. However, collisional excitation of this body in our Solar System is hardly possible because of the rarity of collisions, even in the (not so) dense main asteroid belt[29], and because 1I/'Oumuamua missed the belt at a safe distance and spent very little time close to the ecliptic plane due to the highly inclined orbit and large orbital speed. A sensitive non-detection of a body's debris trail (Fig. 1), starkly contrasting with the prominent, long-lived trail of the similarly sized impacted asteroid P/2010 A2 (ref. [30]), is also not in favour of a very recent collision. Rather, we believe that 1I/'Oumuamua was excited in another planetary system—presumably its home system—in the distant past. The damping time scale of a typical rubble pile asteroid having the same effective size and rotation rate as 1I/'Oumuamua, and the minimum allowable axis ratio, is about 1 Gyr (see Methods). This

appears to be long enough to preserve the signs of collisional excitation over the timescale of a typical interstellar exile[8], supporting our conclusion. Whether 1I/'Oumuamua was produced and excited in a catastrophic collision between larger bodies or subcatastrophically impacted by another small body is unclear, but both scenarios lead to the same conclusion that collisional processing of minor object populations in exoplanetary systems might be common. Supposedly, 1I/'Oumuamua was ejected from its home system with a large number of similar bodies during a period of dynamical instability[1] when frequent collisions would have been expected.

Methods

Observations, data reduction and photometry. The GMOS-N we used to collect data contains three adjacent Hamamatsu charge-coupled devices, providing imaging over a 5.5 × 5.5 arcmin field of view and spectroscopy from 0.36 to 0.94 μm[31].
For the present analysis, we pre-selected imaging data from the central charge-coupled device chip, taken consistently through the broadband r′ filter from the Sloan Digital Sky Survey photometric system[15] with the instrument configured to provide 2 × 2 binning and 0.1614 arcsec effective pixels. The complete time series consists of 438 images with an integration time of 30.0 s, 2 images with a 20.0 s integration time acquired as part of a multi-band sequence, and 2 images with a 10.0 s integration time obtained as part of a spectroscopic acquisition sequence. The data were taken between 7:34:49 and 12:46:23 UT on 27 October 2017 and between 5:52:24 and 12:25:30 UT on 28 October 2017. The sky was photometric and the median zenith seeing close to 0.6 arcsec (in full width at half maximum) throughout the observations. It is practical to anchor data reduction and modelling at one specific epoch, which we chose to be 28 October 2017 at 00:00 UT, close to the middle-point of our run. At this standard epoch, the helio- and geocentric distances of 1I/'Oumuamua were equal to 1.4317 and 0.4963 au, respectively, and the phase angle was 22.93°.
The images were corrected for overscan, bias and flatfield in the standard manner. Then, using our established technique[32], we carefully subtracted a dense background of stars and galaxies interfering with 1I/'Oumuamua as it moved across the sky. To remove the background from a given image, we mean combined
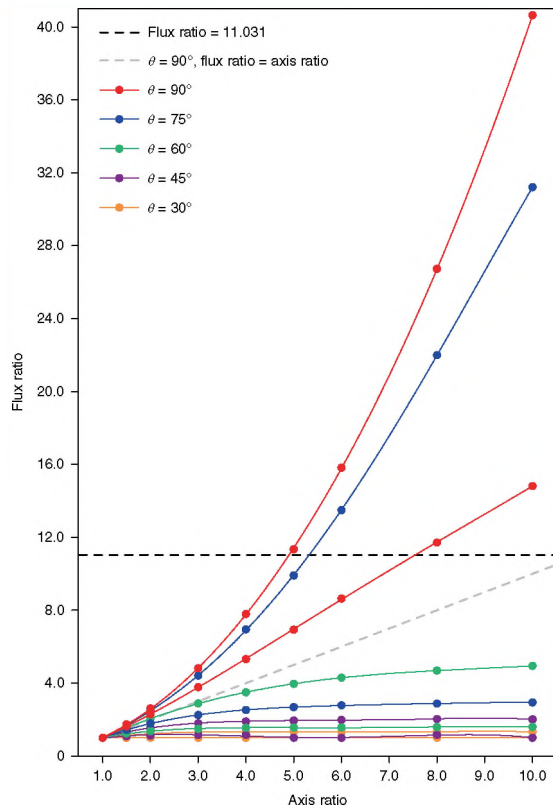
Flux ratio = 11.031

$\theta = 90°$, flux ratio = axis ratio

$\theta = 90°$

$\theta = 75°$

$\theta = 60°$

$\theta = 45°$

$\theta = 30°$

Flux ratio

Axis ratio

Fig. 4 | Results from Hapke modelling applicable to the observing circumstances of 1I/'Oumuamua. The filled coloured symbols show the dependence between the maximum-to-minimum flux ratio and long-to-short axis ratio calculated for a set of aspect angles θ (defined as the angle between the line of sight and the rotation axis). The solid coloured lines are the fourth order polynomial fits added to guide the eye. For each angle θ, two extreme trajectories are presented for different polar angles (orthogonal to θ)—one for the minimum flux ratio and one for the maximum flux ratio. See Methods for details of the computation. The grey dashed line shows a commonly used linear model calculated for $\theta = 90°$ in which the flux ratio is directly equal to the axis ratio. The black dashed line shows the actual flux ratio measured from our 1I/'Oumuamua photometric data.

up to six star-aligned images taken around the same time and subtracted the result of this operation from the affected image. We did not use the nearest images from a consecutive series to avoid contaminating the photometric background annulus with the object's own signal. As a result, we obtained uncontaminated images of the target on a very clean and uniform background suitable for accurate time-resolved photometry. The frames were then visually inspected for artefacts, such as cosmic ray hits and residual signal from imperfect subtraction of bright background objects at a location of 1I/'Oumuamua. This procedure resulted in the rejection of 11 images—a small number compared with the remaining 431 images available for detailed analysis. The restricted dataset has the same time limits as the complete time series, a total temporal coverage of 29,030 s (or 8.06 h) and a total integration time of 12,880 s (or 3.58 h). In this work, we define the total temporal coverage as a sum of observing blocks characterized by negligibly small gaps (not exceeding 300 s) between the end times and start times of consecutive integrations.

The restricted dataset was photometrically measured using the Aperture Photometry Tool[33] configured in mean sky subtraction mode. The brightness of 1I/'Oumuamua, along with photometric uncertainty, were determined from a circular aperture with a constant diameter of 2.26 arcsec (14 pixels), which ensured negligible influence of seeing variations and an acceptable level of background noise contribution. We also made similar measurements of brighter background stars, this time employing a larger aperture of 4.84 arcsec (30 pixels) to account for the elongation of stellar profiles caused by rapid non-sidereal tracking of the target. Instrumental photometry of 1I/'Oumuamua was then corrected for the atmospheric extinction (assuming the standard r′ -band extinction coefficient for Mauna Kea of 0.11 mag airmass⁻¹) and absolute calibrated using a common magnitude zero level determined for our run from the photometry of background stars available in the Sloan Digital Sky Survey photometric catalogue[34]. Apparent magnitudes were then reduced to the standard observing geometry on 28 October 2017 at 00:00 UT, assuming the asteroidal photometric phase function[35] with a parameter $G = 0.15$ characteristic of Solar System C-types[36]. However, the phase component of the geometric correction was very small thanks to the nearly constant phase angle during the observations, and the correction was dominated by the geocentric distance. The same phase function was assumed in the calculation of the absolute median magnitude, but this time the phase component of the correction was significant, reflecting the relatively large value of the phase angle during the observations. The dataset was also corrected for the non-constant travel time of light by subtracting light travel time offsets calculated with respect to the standard epoch of the observations. The light curve expressed in magnitudes was also converted to flux, expressed as a product of the effective wavelength and the wavelength flux density. We measured several parameters of the light curve, including the maximum-to-minimum flux ratio. The extrema were calculated by averaging the five highest fluxes and the five lowest fluxes using inverse-variance weighting.

Periodicity analysis. Periodicity analysis was conducted using the PDM method because this technique is particularly well suited to the analysis of a non-sinusoidal time series of unequally spaced data[14]. The PDM algorithm folds the input data using a range of trial frequencies and examines the quality of data folding using a variance ratio, defined as the effective variance of the data in phase bins normalized by the variance of the unbinned data. The method has two adjustable parameters—the number of independent (adjacent) phase bins N_b and the number of bin covers N_c. The former controls the width of the actual computational bins (equal to $1/N_b$) and the latter controls the overlap of successive computational bins (that is, it specifies how many of them overlap), while both control the total number of computational bins (equal to $N_b \times N_c$). Originally insensitive to data uncertainties[14], the classical PDM was later upgraded to include inverse-variance weighting of the data points[15]—a major improvement, which this study takes full advantage of.

Due to this inverse-variance weighting of the data, we chose for the analysis the time series expressed in flux (and not magnitude), characterized by rather uniform uncertainties, to within a factor of two (see Fig. 2b), thereby ensuring good sensitivity of the method to the entire dataset. As for the light curve expressed in magnitude, the weighted PDM was practically blind to the light curve minima, featuring a factor of approximately ten larger uncertainties than the light curve maxima (Fig. 2b), which severely limited its usefulness for periodicity analysis. The algorithm was run on the data with N_b ranging from 10 to 30 and N_c ranging from 3 to 7, ensuring, on the one hand, good overall statistics in the computational bins (containing on average 43.1 to 14.4 data points, respectively) and, on the other hand, good sensitivity to moderately complex light curves (resolved into 10.0 to 3.3% rotation-phase elements, respectively). Given that for all these settings we obtained consistent results, we present only one representative outcome, calculated using $N_b = 20$ and $N_c = 5$.

Formal uncertainties of the selected periodicity solutions were estimated by propagating the photometric errors using a Monte Carlo method. This was done by generating and analysing 1,000 simulated light curves, each created from the original light curve by adding a random realization of noise. The superimposed variates were calculated individually for each data point, assuming a normal probability distribution with a standard deviation equal to the photometric uncertainty. Then, using again the weighted PDM, we analysed the simulations in narrow frequency windows centred on the investigated periodicity solutions, and from the observed frequency variations about their original values, we derived their standard errors. It is important to realize that the formal uncertainties estimated in this way do not take into account the fact that 1I/'Oumuamua is in a state of non-principal-axis rotation. Consequently, the light curve folded using even the best simple-periodicity solution suffers from excessive scatter of the data points, often significantly exceeding the formal photometric error bars, which was ignored in the present analysis. Moreover, the determined frequency may not work at all for other datasets obtained at different times, even though it has a very small formal uncertainty.

Hapke modelling. Using Hapke's reflectance model[20], we computed simulated light curves for the observing geometry of 1I/'Oumuamua anchored at the standard epoch of our observations, 28 October 2017 at 00:00 UT. We employed the modified isotropic multiple scattering approximation with the shadow-hiding opposition effect and macroscopic roughness influencing reflectance properties. Colorimetric and spectroscopic observations of 1I/'Oumuamua have revealed that the reflectance spectrum of this object is close to those of Solar System C- or D-type asteroids, Trojans or comets[7,8,10,37]. Thus, we adopted a set of literature

values for the reflectance parameters of C-type asteroids[38], such as a single scattering albedo of 0.037, an opposition surge amplitude and width of 0.20 and 0.025, respectively, the asymmetry factor in the Henyey–Greenstein particle phase function equal to –0.47, and an average topographic slope angle of macroscopic roughness of 20°. Furthermore, we defined the spin-axis orientation by the aspect angle (that is, the angle between the spin axis and the line of sight) and the polar angle (measured in the plane perpendicular to the line of sight counterclockwise from the object-Sun direction). For simplicity, we assumed that 1I/'Oumuamua has the shape of a prolate spheroid.

We performed two types of simulation. First, we tested the dependence between the maximum-to-minimum flux ratio and long-to-short axis ratio for a set of spin-axis orientations (Fig. 4). The aspect angle was probed with a step size of 15° and the polar angle was probed with a step size of 22.5°. Second, for a fixed aspect angle of 90° and light curve extrema equal to those measured from our 1I/'Oumuamua data, we investigated the allowable range for the volume-equivalent radius, changing the polar angle with the same step size as before. From the first type of simulation, we found that even an enormous range of brightness variations does not necessarily imply a huge axis ratio. To generate a 2.6 mag rotational amplitude—the same as we observed in our data—an axis ratio can be as low as 4.9, inconsistent with most of the recently published values[6,7,11]. These reported larger axis ratios were calculated under the assumption that flux is proportional to the instantaneous projected cross section, but this can be far from reality for large phase angles and significant shape elongations, when shadowing effects as well as asymmetry of the phase function have a strong influence on an observed light curve. Our approach is more accurate in that it takes the aforementioned factors into account. Moreover, we have found that for aspect angles smaller than about 65° it is virtually impossible to obtain a maximum-to-minimum flux ratio consistent with 1I/'Oumuamua, in spite of blowing up the axis ratio to abnormal values. Thus, we conclude that the aspect angle must be larger than 65°. Finally, from the second type of simulation, we found the volume-equivalent radius in a relatively narrow range from 75 to 79 m (depending on the polar angle and thus the axis ratio) for the assumed model parameters.

Density estimation. The minimum bulk density that ensures rotational stability in the absence of material strength can be calculated from the rotation period and the lower limit to the axis ratio. For simplicity, we neglect the excitation of 1I/'Oumuamua's rotation state, assuming that the body rotates around the shortest axis with a rotation period P. From the exact formula for the shortest tolerable rotation period of a prolate spheroid[32,39], we find that the density ρ_p satisfies:

$$\rho_P \geq \frac{3\pi}{GP^2} \left[\frac{2}{3} \frac{\phi_P^3}{(1-\phi_P^2)\left[\ln\left(\frac{1+\phi_P}{1-\phi_P}\right)-2\phi_P\right]} \right] \tag{1}$$

where $G = 6.67384 \times 10^{-11}$ m^3 kg^{-1} s^{-2} is the gravity constant, and $\phi_P = \sqrt{1-1/f^2}$ is a function of the long-to-short axis ratio f. Note that the term in the outer bracket approaches unity for a sphere and is commonly approximated by f (ref. [18]). The approximation works well for small axis ratios (it is good to 5% for f between 1.0 and 3.0), but introduces significant (and unnecessary) errors for large axis ratios, resulting in underestimated density limits (for example, the full term in the outer bracket is almost 20% larger for $f = 5$ and over 60% larger for $f = 10$). Moreover, the term in the outer bracket is a monotonically increasing function of f, implying that the above inequality is also naturally satisfied if we replace the actual value of f with the lower limit on f. Substituting the measured rotation period and axis-ratio limit of 1I/'Oumuamua, equal to 7.56 h and 4.9, respectively, we find $\rho_p \geq 1,100$ kg m^{-3}. The density limit for an oblate shape is even less stringent, as in this case we find $\rho_o \geq 500$ kg m^{-3}, calculated from[39]:

$$\rho_o \geq \frac{3\pi}{GP^2} \left[\frac{2}{3} \frac{\phi_o^3}{(1+\phi_o^2)\arctan(\phi_o)-\phi_o} \right] \tag{2}$$

where $\phi_o = \sqrt{f^2-1}$ is a different function of the long-to-short axis ratio f. The term in the outer bracket is again a monotonically increasing function of f and again approaches unity for a sphere, but can no longer be approximated with f (except for nearly spherical shapes).

The same approach was also used by other teams[6,7,10,11], who reported the density limit estimated from the rotation periods and axis-ratio limits extracted from their data. However, with one prominent exception[10], they obtained grossly overestimated values ranging from $\rho_p \geq 5,000$ kg m^{-3} to $\rho_p \geq 20,000$ kg m^{-3} (interpreted as an indication of non-negligible tensile strength). The reason for this is threefold. First, the overly simplistic treatment of the light curve resulted in overestimated axis-ratio limits (see before), up to a factor of about two[6] or less where the light curve range was not fully recovered[7,11]. Second, the teams used the simplified version of equation (1), which actually somewhat reduced the density overestimation. Finally, and most significantly, the formula they used contains

an error in the axis ratio f, which is introduced as a square term but should be a linear term.

Damping timescale estimation. The damping (or relaxation) timescale τ_d can be written as[38,40]:

$$\tau_d = \frac{P^3}{C^3 D^2} \tag{3}$$

where P is the measured 'effective' rotation period, D is the volume-equivalent diameter and C is a function of shape (or axis ratios for an ellipsoid approximation), material (density, stiffness and quality factor) and rotation (maximum and minimum wobble angle). The most recent[38] estimates find $C \sim 3.6 \times 10^1$ h Gyr$^{-\frac{1}{3}}$ km$^{-\frac{4}{3}} \sim 4.1 \times 10^{-3}$ s$^{\frac{2}{3}}$ m$^{-\frac{4}{3}}$ for typical properties of Solar System asteroids. Substituting this value and the measured rotation period and diameter of 1I/'Oumuamua, equal to 7.56 h and 154 m, respectively, we find $\tau_d \sim 0.4$ Gyr. However, the real damping timescale of this object is significantly longer because 1I/'Oumuamua has a much more extreme shape than that adopted in the estimation of C and the value of this parameter decreases with the axis ratio[41,42]. Hence, our conservative order-of-magnitude estimate for 1I/'Oumuamua's damping timescale is 1 Gyr, but it can be much longer if, for example, the axis ratio is significantly greater than the measured lower limit of 4.9.

References

1. Woolum, D. S. & Cassen, P. M. in *Encyclopedia of the Solar System* (eds Weissman, P. R., McFadden, L.-A. & Johnson, T. V.) 27–28 (Academic Press, San Diego, 1999).
2. Moro-Martín, A., Turner, E. L. & Loeb, A. Will the large synoptic survey telescope detect extra-solar planetesimals entering the Solar System? *Astrophys. J.* **704**, 733–742 (2009).
3. Sekanina, Z. A probability of encounter with interstellar comets and the likelihood of their existence. *Icarus* **27**, 123–133 (1976).
4. Stern, S. A. On the number density of interstellar comets as a constraint on the formation rate of planetary systems. *Publ. Astron. Soc. Pac.* **102**, 793–795 (1990).
5. Williams, G. *MPEC 2017-U181: Comet C/2017 U1 (PANSTARRS)* (International Astronomical Union, 2017); https://www.minorplanetcenter.net/mpec/K17/K17U11.html.
6. Meech, K. J. et al. A brief visit from a red and extremely elongated interstellar asteroid. *Nature* **552**, 378–381 (2017).
7. Jewitt, D. et al. Interstellar interloper 1I/2017 U1: observations from the NOT and WIYN telescopes. *Astrophys. J. Lett.* **850**, L36 (2017).
8. Ye, Q.-Z., Zhang, Q., Kelley, M. S. P. & Brown, P. G. 1I/2017 U1 ('Oumuamua) is hot: imaging, spectroscopy, and search of meteor activity. *Astrophys. J. Lett.* **851**, L5 (2017).
9. Knight, M. M. et al. On the rotation period and shape of the hyperbolic asteroid 1I/'Oumuamua (2017 U1) from its lightcurve. *Astrophys. J. Lett.* **851**, L31 (2017).
10. Bolin, B. T. et al. APO time-resolved color photometry of highly elongated interstellar object 1I/'Oumuamua. *Astrophys. J. Lett.* **852**, L2 (2018).
11. Bannister, M. T. et al. Col-OSSOS: colors of the interstellar planetesimal 1I/'Oumuamua. *Astrophys. J. Lett.* **851**, L38 (2017).
12. Feng, F. & Jones, H. R. A. 'Oumuamua as a messenger from the local association. *Astrophys. J. Lett.* **852**, L27 (2018).
13. Fukugita, M. et al. The Sloan Digital Sky Survey photometric system. *Astron. J.* **111**, 1748–1756 (1996).
14. Stellingwerf, R. F. Period determination using phase dispersion minimization. *Astrophys. J.* **224**, 953–960 (1978).
15. Drahus, M. & Waniak, W. Non-constant rotation period of comet C/2001 K5 (LINEAR). *Icarus* **185**, 544–557 (2006).
16. Fitzsimmons, A. et al. Spectroscopy and thermal modelling of the first interstellar object 1I/2017 U1 'Oumuamua. *Nat. Astron.* **2**, 133–137 (2018).
17. Fraser, W. C. et al. The tumbling rotational state of 1I/'Oumuamua. *Nat. Astron.* https://doi.org/10.1038/s41550-018-0398-z (2018).
18. Pravec, P. & Harris, A. W. Fast and slow rotation of asteroids. *Icarus* **148**, 12–20 (2000).
19. Warner, B. D., Harris, A. W. & Pravec, P. The asteroid Lightcurve Database. *Icarus* **202**, 134–146 (2009).

LETTERS

20. Hapke, B. *Theory of Reflectance and Emittance Spectroscopy* (Cambridge University Press, New York, 2012).
21. Hilton, J. L. in *Asteroids III* (eds Bottke, W. F. et al.) 103–112 (University of Arizona Press, Tucson, 2002).
22. Pravec, P. et al. Tumbling asteroids. *Icarus* **173**, 108–131 (2005).
23. Samarasinha, N. H. Rotational excitation and damping as probes of interior structures of asteroids and comets. *Meteorit. Planet. Sci.* **43**, 1063–1073 (2008).
24. Belton, M. J. S., Julian, W. H., Anderson, A. J. & Mueller, B. E. A. The spin state and homogeneity of comet Halley's nucleus. *Icarus* **93**, 183–193 (1991).
25. Belton, M. J. S. et al. The complex spin state of 103P/Hartley 2: kinematics and orientation in space. *Icarus* **222**, 595–609 (2013).
26. Hudson, R. S. & Ostro, S. J. Shape and non-principal axis spin state of asteroid 4179 Toutatis. *Science* **270**, 84–86 (1995).
27. Samarasinha, N. H., Mueller, B. E. A., Belton, M. J. S. & Jorda, L. in *Comets II* (eds Festou, M., Keller, H. U. & Weaver, H. A.) 281–299 (University of Arizona Press, Tucson, 2004).
28. Pravec, P. et al. The tumbling spin state of (99942) Apophis. *Icarus* **233**, 48–60 (2014).
29. Bottke, W. F. et al. Linking the collisional history of the main asteroid belt to its dynamical excitation and depletion. *Icarus* **179**, 63–94 (2005).
30. Kim, Y., Ishiguro, M., Michikami, T. & Nakamura, A. M. Anisotropic ejection from active asteroid P/2010 A2: an implication of impact shattering on an asteroid. *Astron. J.* **153**, 228 (2017).
31. Hook, I. M. et al. The Gemini-North Multi-Object Spectrograph: performance in imaging, long-slit, and multi-object spectroscopic modes. *Publ. Astron. Soc. Pac.* **116**, 425–440 (2004).
32. Drahus, M. et al. Fast rotation and trailing fragments of the active asteroid P/2012 F5 (Gibbs). *Astrophys. J. Lett.* **802**, L8 (2015).
33. Laher, R. R. et al. Aperture photometry tool. *Publ. Astron. Soc. Pac.* **124**, 737–763 (2012).
34. Eisenstein, D. J. et al. SDSS-III: massive spectroscopic surveys of the distant Universe, the Milky Way, and extra-solar planetary systems. *Astron. J.* **142**, 72 (2011).
35. Bowell, E. et al. in *Asteroids II* (eds Binzel, R. & Gehrels, T.) 524–556 (University of Arizona Press, Tucson, 1989).
36. Luu, J. & Jewitt, D. On the relative numbers of C types and S types among near-earth asteroids. *Astron. J.* **98**, 1905–1911 (1989).
37. Masiero, J. Palomar optical spectrum of hyperbolic near-earth object A/2017 U1. Preprint at https://arxiv.org/abs/1710.09977 (2017).
38. Helfenstein, P. & Veverka, J. in *Asteroids II* (eds Binzel, R. & Gehrels, T.) 557–593 (University of Arizona Press, Tucson, 1989).
39. Davidsson, B. J. R. Tidal splitting and rotational breakup of solid biaxial ellipsoids. *Icarus* **149**, 375–383 (2001).
40. Pravec, P., Harris, A. W. & Michalowski, T. in *Asteroids III* (eds Bottke, W. F. et al.) 113–122 (University of Arizona Press, Tucson, 2002).
41. Sharma, I., Burns, J. A. & Hui, C.-Y. Nutational damping times in solids of revolution. *Mon. Not. R. Astron. Soc.* **359**, 79–92 (2005).
42. Breiter, S., Rożek, A. & Vokrouhlický, D. Stress field and spin axis relaxation for inelastic triaxial ellipsoids. *Mon. Not. R. Astron. Soc.* **427**, 755–769 (2012).

Author contributions
P.G. suggested the target. M.D., P.G., B.H. and S.K. designed the observations and wrote the telescope time proposal. P.G. and M.D. carried out the image cleaning and photometry. W.W. reduced the raw images and performed light curve modelling. M.D. led data analysis and writing of the paper with contributions from P.G. and W.W., S.X. assisted in proposal writing and organization of the observations. All authors checked the work and proofread the paper.

Competing interests
The authors declare no competing interests.

Additional information
Supplementary information is available for this paper at https://doi.org/10.1038/s41550-018-0440-1.

Reprints and permissions information is available at www.nature.com/reprints.

Correspondence and requests for materials should be addressed to M.D. or P.G.

Publisher's note: Springer Nature remains neutral with regard to jurisdictional claims in published maps and institutional affiliations.

Initial characterization of interstellar comet 2I/Borisov

Piotr Guzik [1,7*], Michał Drahus [1,7*], Krzysztof Rusek[2], Wacław Waniak [1], Giacomo Cannizzaro [3,4] and Inés Pastor-Marazuela [5,6]

Interstellar comets penetrating through the Solar System had been anticipated for decades[1,2]. The discovery of asteroidal-looking 'Oumuamua[3,4] was thus a huge surprise and a puzzle. Furthermore, the physical properties of the 'first scout' turned out to be impossible to reconcile with Solar System objects[4-6], challenging our view of interstellar minor bodies[7,8]. Here, we report the identification and early characterization of a new interstellar object, which has an evidently cometary appearance. The body was discovered by Gennady Borisov on 30 August 2019 UT and subsequently identified as hyperbolic by our data mining code in publicly available astrometric data. The initial orbital solution implies a very high hyperbolic excess speed of ~32 km s^{-1}, consistent with 'Oumuamua[9] and theoretical predictions[2,7]. Images taken on 10 and 13 September 2019 UT with the William Herschel Telescope and Gemini North Telescope show an extended coma and a faint, broad tail. We measure a slightly reddish colour with a g'−r' colour index of 0.66 ± 0.01 mag, compatible with Solar System comets. The observed morphology is also unremarkable and best explained by dust with a power-law size-distribution index of −3.7 ± 1.8 and a low ejection speed (44 ± 14 m s^{-1} for $\beta = 1$ particles, where β is the ratio of the solar gravitational attraction to the solar radiation pressure). The nucleus is probably ~1 km in radius, again a common value among Solar System comets, and has a negligible chance of experiencing rotational disruption. Based on these early characteristics, and putting its hyperbolic orbit aside, 2I/Borisov appears indistinguishable from the native Solar System comets.

On 8 September 2019 at 04:15 universal time (UT), we were alerted by our software Interstellar Crusher (see Methods) of a possible new hyperbolic object gb00234. Within less than 4 d, the orbit became reliable enough to trigger the first announcements[10,11], and subsequently, the body received an official name 2I/Borisov. As of 20 September 2019 at 12:00 UT, 447 published astrometric positions collected over a 21.1 d interval[11-15] are demonstrably incompatible with a parabolic orbit (Fig. 1). In the absence of non-gravitational forces, the residuals show a very strong systematic trend and reach up to 20 arcsec. Inclusion of non-gravitational forces greatly reduces the residuals, but a small systematic trend is still present. More importantly, the resulting non-gravitational accelerations $A_1 = 7.43 \pm 0.07 \times 10^{-4}$ au d^{-2} and $A_2 = -1.83 \pm 0.01 \times 10^{-4}$ au d^{-2} given at 1 au from the Sun (see Methods) are implausibly high, exceeding the largest measured non-gravitational accelerations of comets[16] by two to three orders of magnitude and comparable to the

sunward gravitational acceleration at 1 au. However, the data are accurately fitted by an unrestricted, purely gravitational solution (Fig. 1) that implies a strongly hyperbolic orbit with an eccentricity of 3.38 ± 0.02 (Table 1). This strong hyperbolicity cannot be attributed to gravitational perturbations from the Solar System's planets because the body travels from a direction far from the ecliptic plane. Thus, the only viable explanation is the arrival from outside the Solar System. The huge eccentricity together with a moderate perihelion distance of 2.012 ± 0.004 au (Table 1) imply a hyperbolic excess speed of ~32 km s^{-1}. The body entered the Solar System from a direction ~75° away from the Solar apex with the asymptotic radiant at J2000.0 right ascension (RA) = 02 h 12 m and declination (dec) = 59.4° in the constellation of Cassiopeia. For the most up-to-date orbital parameters, readers are referred to the online databases of the Minor Planet Center or Jet Propulsion Laboratory.

We observed this object using the 4.2 m William Herschel Telescope (WHT) on La Palma and the 8.2 m Gemini North Telescope at Maunakea in the Sloan Digital Sky Survey (SDSS) g' and r' bands[17]. WHT data were obtained with the Auxiliary-port CAMera (ACAM) on 10 September 2019 at 05:38 UT and on 13 September 2019 at 05:47 UT (observation mid-points). The first set comprises ten sidereal-tracked 60 s exposures, of which five were obtained in the g' band and five in the r' band, whereas the second set contains 40 sidereal-tracked 20 s exposures, 20 obtained in g' and 20 in r'. Gemini data were collected with the Gemini Multi-Object Spectrograph (GMOS-N) on 10 September 2019 at 14:57 UT (mid-point) with non-sidereal tracking and comprise four g'-band and four r'-band exposures taken with 60 s integration time. The datasets were obtained at low elevation (22° to 31°) in morning twilight (solar elevation from −19° to −12°). At the time of the observations, the helio- and geocentric distances of 2I/Borisov were equal to 2.8 and 3.4 au, respectively, the phase angle was ~15° and the apparent motion was ~75 arcsec h^{-1}. The images were corrected for overscan, bias and flatfield in the standard fashion, and then a global background level was subtracted from each frame.

In Fig. 2 we show median-stacked g'-band and r'-band images from Gemini, which have a better signal-to-noise ratio than the WHT images. The latter are presented in Supplementary Fig. 1. The images reveal an extended coma and a broad, short tail emanating in roughly antisolar direction. We see no clear difference in morphology in the two bands. The comet was measured photometrically in each individual exposure from the two telescopes and two nights. We consistently used a 5,000 km (~2 arcsec) radius photometric aperture and determined the brightness against background

[1]Astronomical Observatory, Jagiellonian University, Kraków, Poland. [2]AGH University of Science and Technology, Kraków, Poland. [3]SRON, Netherlands Institute for Space Research, Utrecht, the Netherlands. [4]Department of Astrophysics/IMAPP, Radboud University, Nijmegen, the Netherlands. [5]Anton Pannekoek Institute for Astronomy, University of Amsterdam, Amsterdam, the Netherlands. [6]ASTRON, Netherlands Institute for Radio Astronomy, Dwingeloo, the Netherlands. [7]These authors contributed equally: Piotr Guzik, Michał Drahus. *e-mail: piotr.guzik@doctoral.uj.edu.pl; drahus@oa.uj.edu.pl
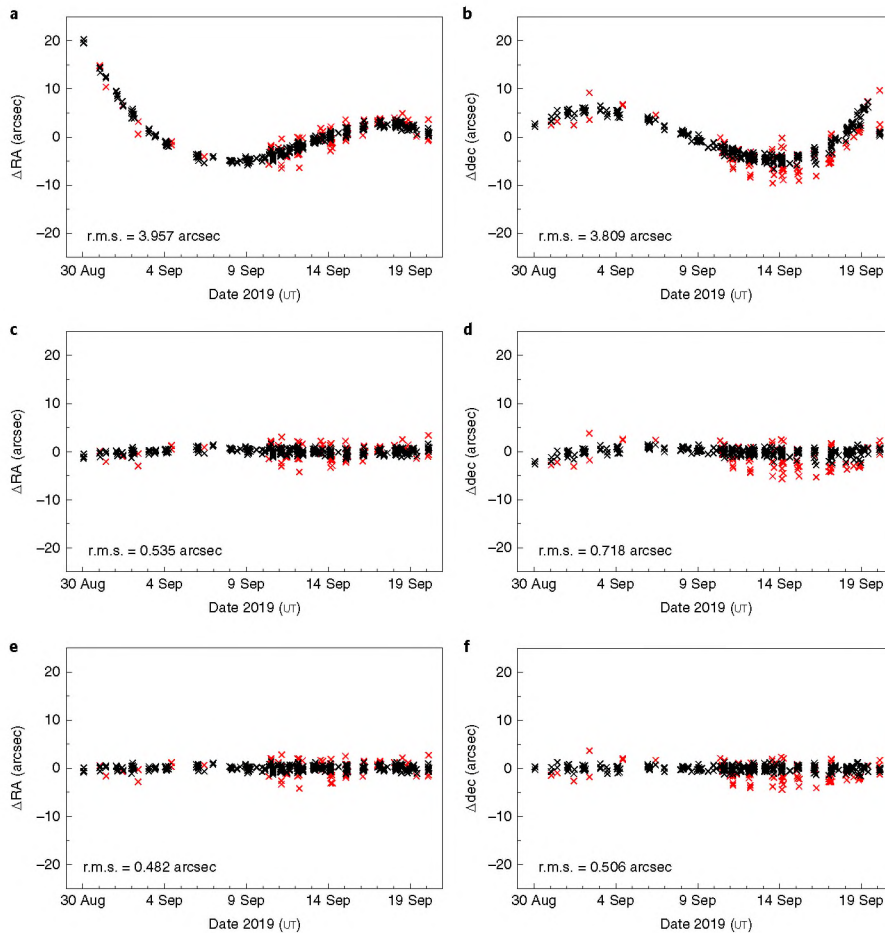
Fig. 1 | Astrometric residuals of 2I/Borisov calculated for three different orbital solutions. a,b, The residuals calculated for a parabolic solution without non-gravitational forces. **c,d,** The residuals for a parabolic solution with non-gravitational forces. **e,f,** The residuals for an unrestricted solution without non-gravitational forces. Residuals are presented separately in RA (**a,c,e**) and dec (**b,d,f**). Black symbols denote data used in the computation and red symbols denote rejected outliers. r.m.s., root mean squared.

Table 1 | Hyperbolic heliocentric orbital elements of 2I/Borisov calculated for the osculation epoch 2019 September 20.0 TT

Date of perihelion passage, T	2019 December 8.42 ± 0.11 TT
Orbital eccentricity, e	3.3790 ± 0.020
Perihelion distance, q	2.0119 ± 0.0044 au
Argument of perihelion, ω	209.001 ± 0.100° (J2000.0)
Longitude of ascending node, Ω	308.195 ± 0.040° (J2000.0)
Inclination, i	44.004 ± 0.041° (J2000.0)

All errors are 1 standard deviation.

stars available in the SDSS photometric catalogue[18]. As a result, we obtained dataset-averaged AB magnitudes $g' = 19.38 \pm 0.01$ and $r' = 18.71 \pm 0.01$ for the WHT observations on 10 September 2019 at 05:38 UT, $g' = 19.38 \pm 0.01$ and $r' = 18.72 \pm 0.01$ for the

Gemini observations on 10 September 2019 at 14:57 UT, and $g' = 19.32 \pm 0.02$ and $r' = 18.67 \pm 0.01$ for the WHT observations on 13 September 2019 at 05:47 UT. Photometric magnitudes can be used to estimate the nucleus size. Following two independent approaches, we have found that the nucleus of 2I/Borisov is most likely ~1 km in radius (see Methods). However, it should be noted that these approaches are inherently very uncertain. Our photometric measurements give a consistent $g'-r'$ colour index, with an average value of 0.66 ± 0.01 mag. The colour is slightly redder than the solar $g'-r' = 0.45 \pm 0.02$ mag (ref. [19]) and implies a positive spectral slope $S' \sim 12.5\%$ per 100 nm (see Methods), in good agreement with an independent spectroscopic determination[20]. Within the errors, the same colour is obtained for other photometric apertures as well (we made measurements for the apertures ranging from 3,000 to 15,000 km in radius), implying a uniform colour of the coma. This, and the similarity of morphology in both bands, are both indicative of dust-dominated activity in our data. Monte Carlo modelling of the object's dust environment with our established code[21] has revealed

NATURE ASTRONOMY   **LETTERS**
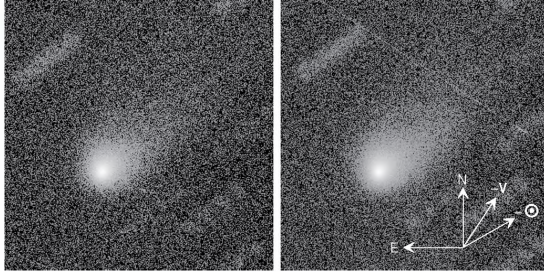

Fig. 2 | Median-stacked images of 2I/Borisov from Gemini North. The left panel shows the image in the g′ band and the right panel shows the image in the r′ band. Both panels subtend 1.0 × 1.0 arcmin and were scaled logarithmically. Arrows show the directions of north (N) and east (E), the projected antisolar vector (-☉) and the negative of the orbital velocity vector (-**V**). The pixel scale is 0.16 arcsec px⁻¹ and the seeing was 1.8 arcsec.

a power-law particle size-distribution exponent of −3.7 ± 1.8 and a 44 ± 14 m s⁻¹ ejection speed applicable to $\beta = 1$ particles (where β is the ratio of the solar gravitational attraction to the solar radiation pressure; see Methods).

The dynamical properties and morphology of 2I/Borisov make it clear that the body is the first certain case of an interstellar comet, and the second known interstellar minor body identified in the Solar System (after 'Oumuamua[3,4]). Evidently, the extended coma and the broad tail stand in stark contrast with the purely asteroidal appearance of 'Oumuamua. The estimated nucleus size is common among Solar System's comets[22,23]. Adopting the formalism of rotational disruption probability[24] and assuming typical properties of Solar System comets, we have estimated the probability of rotational disruption during the Solar System flyby to be smaller than 1% (see Methods). The measured colour is consistent with the colours of the Solar System's comets[25,27] and falls only slightly redwards of the median and average values of the observed g′-r′ distribution (Fig. 3). The same similarity can be noticed for the dust coma parameters[28,29]. These facts are remarkable in and of themselves, and especially remarkable after 'Oumuamua, the multiple peculiarities of which[4-6] prompted us to rethink our entire view of the nature of interstellar interlopers[7]. However, 2I/Borisov appears completely similar to the native Solar System's comets.

Comet 2I/Borisov was discovered on its way to perihelion (8 December 2019 UT at 2.0 au) and before the closest approach to Earth (28 December 2019 UT at 1.9 au); thus, the overall visibility will be gradually improving. The body is destined for an intensive observing campaign lasting many months (Supplementary Fig. 2) that will allow us to gain groundbreaking insights into the physical properties of interstellar comets and exosolar planetary systems in general. This discovery is in line with the detection statistic of one interstellar object per year proposed by several authors[30,31] after the discovery of 'Oumuamua, which is an order of magnitude higher than the most optimistic pre-'Oumuamua estimates[32]. It also shows that cometary nature of these bodies might be a common characteristic, in agreement with the original expectations[1,2]. More discoveries are expected in the near future thanks to the Large Synoptic Survey Telescope.

Methods

Interstellar Crusher. Interstellar Crusher is a custom Python3 code running on Windows Subsystem for Linux. It continuously monitors the Possible Comet Confirmation Page and computes orbits of newly discovered minor bodies using Bill Gray's Find_Orb (https://github.com/Bill-Gray/find_orb/commit/abe3f5847aad4c39f1d82239bf343c876b3d1bd0). Detection of a possible interstellar object triggers an alarm that is sent via e-mail.
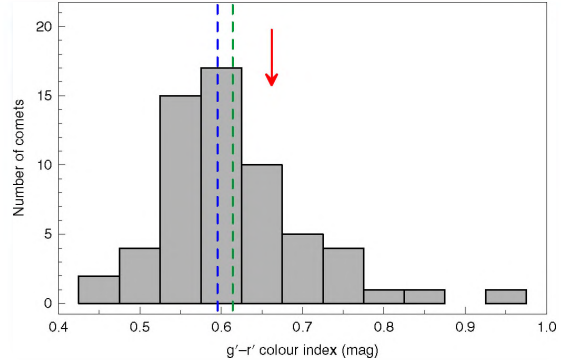

Fig. 3 | Colour of 2I/Borisov in the context of Solar System comets. The histogram shows the g′-r′ colour index distribution for 60 comets[25-27] (long-period, Jupiter-family and active Centaurs). It was calculated from the colour indices reported in the Johnson–Cousins (UBVR$_c$I$_c$) and the original SDSS (ugriz) photometric systems using standard transformation formulae[26,45]. Whenever available, multiple measurements of a single object were filtered and combined to minimize the colour uncertainty. The sample has an r.m.s. error of g′-r′ equal to 0.036 mag and the error does not exceed 0.075 mag for any object (the latter criterion resulted in the rejection of three comets). Dashed lines show the median (blue) and average (green) values of the distribution, and the red arrow indicates the measured g′-r′ colour index of 2I/Borisov.

Orbit. We computed the orbit using Bill Gray's Find_Orb with planetary perturbations. The initial input dataset comprised 447 astrometric positions obtained at 45 different stations that were publicly available as of 20 September 2019 at 12:00 UT. We computed parabolic and unrestricted solutions without non-gravitational forces and a parabolic solution with non-gravitational forces defined according to the standard Marsden–Sekanina model[35]. Given the absence of reliable uncertainties of individual observations, we assumed equal weights. Astrometric positions with residuals greater than 1.5 arcsec with respect to the unrestricted solution without non-gravitational forces were iteratively rejected, resulting in a restricted dataset of 362 measurements. This dataset was used for the final computations, the results of which are presented in Fig. 1 and Table 1. The reported uncertainties of the orbital elements were estimated by the least squares method from the astrometric residuals.

Photometry and colour. Individual calibrated exposures were first scrutinized for background stars, cosmic-ray hits and other artefacts in the comet's photometric aperture. As a result of this procedure, we rejected one g′-band frame from the Gemini dataset, one g′-band and one r′-band frame from the first WHT dataset, and accepted all frames from the second WHT dataset. For each dataset, we identified a set of field stars available in the SDSS photometric catalogue[36] that were brighter than the comet and had a g′-r′ colour index between 0.3 and 1.0 mag. We identified 7 and 9 suitable stars for the first and second WHT dataset, respectively, and 4 stars for the Gemini dataset. Photometric measurements of the comet were done using a circular aperture with a 5,000 km (~2.0 arcsec) radius. The stars were measured in a larger, 4.0 arcsec radius aperture that contained >99% of the flux (determined from the curve of growth). Sky background level was estimated (as a mean value) in an annular aperture with a radius of 7.0–9.0 arcsec for the comet and 5.0–8.0 arcsec for the stars. We masked the regions of the background aperture contaminated by the comet's tail, faint field stars and cosmic-ray hits. Centroids were measured from a 1.0 arcsec radius aperture. Differential magnitudes of the comet were calculated for each individual image and then dataset averaged (with equal weights) and compared with the SDSS catalogue magnitudes of the reference stars. The photometric uncertainties were propagated from the individual differential measurements and SDSS uncertainties of the reference stars.

Colour index ($m_1 − m_2$) can be easily converted to the normalized reflectance slope S′. By definition

$$(m_1 - m_2) - (m_1 - m_2)_\odot = -2.5 \log(S_1/S_2)$$

where $(m_1 − m_2)_\odot$ is the solar colour index, $S_i = 1 + S'(\lambda − \lambda_0)/\Delta\lambda_i$ is the normalized reflectance at wavelength λ, $\Delta\lambda_i$ defines the standard wavelength interval of S′ and λ_0 is the normalization wavelength. Using the customary values $\lambda_0 = 550$ nm and $\Delta\lambda_i = 100$ nm, and substituting the measured g′-r′ colour index of

comet 2I/Borisov equal to 0.66 mag along with the effective filter wavelengths $\lambda_g = 475$ nm and $\lambda_r = 630$ nm and the solar $g'-r' = 0.45$ mag (ref. [19]), we calculated the corresponding slope $S' = 12.5\%$ per 100 nm.

Nucleus size estimation. To estimate the size of the nucleus, we followed a simple approach[2] that connects theoretical sublimation rate of water from a unit surface area[34] with an empirical correlation of the observed total visual magnitudes with the total water production rates[35]. By solving the standard energy budget equation[34] with an assumed Bond albedo of 4% and emissivity of 100%, we find that the average water sublimation flux from a spherical non-rotating nucleus is 1.86×10^{26} molecules s^{-1} km^{-2} at the heliocentric distance applicable to our observations. From our Gemini data, we estimate the total visual magnitude to be ~17.5, which is the asymptotic magnitude from the curve of growth transformed from the SDSS g' and r' bands to the Johnson Vband[36]. Taking into account the geo- and heliocentric distances at the time of the observation, this magnitude corresponds to the water production rate of ~10^{27} molecules s^{-1} according to an empirical relation[35]. By comparing the theoretical and observed water production rates, we estimate the area of the sublimating surface to be ~5 km^2, which corresponds to ~1 km radius nucleus with 30% active fraction, assuming negligible contribution of icy grains in the coma.

The same result is obtained from a comparison of 2I/Borisov with the well-studied comet Hale–Bopp in terms of the Afρ parameter[37]. From our r'-band magnitudes measured in the 5,000 km radius aperture, we calculate Afρ ~ 100 cm, and similar for other aperture sizes. The Afρ of comet Hale–Bopp was ~10,000 cm at the heliocentric distance and phase angle compatible with our observations[38]. Simple scaling of the ~30 km in radius nucleus of the latter comet[39] suggests the nucleus radius of 2I/Borisov of ~ 1 km.

Probability of rotational disruption. Rotational disruption occurs when the nucleus rotation rate becomes too high for the self-gravity and tensile strength to keep the body intact[40]. The probability of disruption P has been formulated[24] as the ratio of the expected change in the rotation frequency $\Delta\omega$ to the total extent of tolerable frequency regime, limited by the negative and positive critical frequency ω_{crit}. Thus

$$P = \frac{\Delta\omega}{2\omega_{crit}}$$

The two components of this equation can be calculated in a relatively straightforward manner using standard formulae[5,41–44]. Substituting in these formulas the estimated nucleus radius of ~ 1 km and adopting typical properties of Solar System comets[23], we find the probability of rotational disruption of 2I/Borisov to be <1%.

Dust modelling. We modelled the dust environment of 2I/Borisov using a Monte Carlo approach[21]. The simulations were done with 2×10^6 power-law distributed dust particles spanning a size range a from 0.5 μm to 1 mm. We assumed the density of the dust material to be 1,000 kg m^{-3}, the scattering efficiency for radiation pressure to be 1.0 and a size-dependent dust ejection speed (at the boundary of the collisional zone) $v_e \propto a^{-0.5}$. The dust emission rate is assumed to be inversely proportional to the square of the heliocentric distance with the earliest particles ejected 70 d before the observation. Under these assumptions, we investigated three different ejection patterns: (1) isotropic; (2) into the subsolar hemisphere with the emission rate proportional to the cosine of the solar zenith distance; and (3) into a sunward conical jet with an opening angle of 30° and a constant intensity. The model was fitted to our highest signal-to-noise ratio r'-band image created from the Gemini data (Fig. 2). The best fit was obtained for the hemispheric pattern (Supplementary Fig. 3), though the fit of the isotropic emission is nearly as good. As a result of this procedure, we retrieved a power-law particle size-distribution exponent of −3.7 ± 1.8 and the ejection speed for particles of a given size, equal to 44 ± 14 m s^{-1} for $\beta = 1$ ($a = 1.2$ μm).

Data availability

The ACAM data are available from the corresponding authors upon reasonable request. The GMOS-N raw data will be available in the Gemini Observatory archive at https://archive.gemini.edu after the expiration of the 12 month proprietary period.

References

1. Sekanina, Z. A probability of encounter with interstellar comets and the likelihood of their existence. *Icarus* **27**, 123–133 (1976).
2. Engelhardt, T. et al. An observational upper limit on the interstellar number density of asteroids and comets. *Astron. J.* **153**, 133 (2017).
3. Williams, G. MPEC 2017-U181: Comet C/2017 U1 (PanStarrs). *IAU Minor Planet Center* https://www.minorplanetcenter.net/mpec/K17/K17U11.html (2017).
4. Meech, K. J. et al. A brief visit from a red and extremely elongated interstellar asteroid. *Nature* **552**, 378–381 (2017).
5. Drahus, M. et al. Tumbling motion of 1I/'Oumuamua and its implications for the body's distant past. *Nat. Astron.* **2**, 407–412 (2018).
6. Micheli, M. et al. Non-gravitational acceleration in the trajectory of 1I/2017 U1 ('Oumuamua). *Nature* **559**, 223–226 (2018).
7. The 'Oumuamua ISSI Team. The natural history of 'Oumuamua. *Nat. Astron.* **3**, 594–602 (2019).
8. Bialy, S. & Loeb, A. Could solar radiation pressure explain 'Oumuamua's peculiar acceleration? *Astrophys. J. Lett.* **868**, L1 (2018).
9. Mamajek, E. Kinematics of the interstellar vagabond 1I/'Oumuamua (A/2017 U1). *Res. Notes AAS* **1**, 21 (2017).
10. Guzik, P. et al. Interstellar comet gb00234. *Astronomer's Telegram* 13100 (2019); http://www.astronomerstelegram.org/?read=13100
11. MPEC 2019-R106: Comet C/2019 Q4 (Borisov). *IAU Minor Planet Center* https://www.minorplanetcenter.net/mpec/K19/K19RA6.html (2019).
12. MPEC 2019-R113: Comet C/2019 Q4 (Borisov). *IAU Minor Planet Center* https://www.minorplanetcenter.net/mpec/K19/K19RB3.html (2019).
13. MPEC 2019-S03: Comet C/2019 Q4 (Borisov). *IAU Minor Planet Center* https://www.minorplanetcenter.net/mpec/K19/K19S03.html (2019).
14. MPEC 2019-S09: Comet C/2019 Q4 (Borisov). *IAU Minor Planet Center* https://www.minorplanetcenter.net/mpec/K19/K19S09.html (2019).
15. MPEC 2019-S25: Comet C/2019 Q4 (Borisov). *IAU Minor Planet Center* https://www.minorplanetcenter.net/mpec/K19/K19S25.html (2019).
16. Sekanina, Z. & Kracht, R., Preperihelion outbursts and disintegration of comet C/2017 S3 (Pan-STARRS). Preprint at https://arxiv.org/abs/1812.07054 (2018).
17. Fukugita, M. et al. The Sloan Digital Sky Survey photometric system. *Astron. J.* **111**, 1748–1756 (1996).
18. Abazajian, K. N. et al. The seventh data release of the Sloan Digital Sky Survey. *Astrophys. J. Suppl. Ser.* **182**, 543–558 (2009).
19. Holmberg, J., Flynn, C. & Portinari, L. The colours of the Sun. *Mon. Not. R. Astron. Soc.* **367**, 449–453 (2006).
20. De León, J. et al. A physical characterization of comet C/2019 Q4 (Borisov) with OSIRIS at the 10.4 m GTC. *Res. Notes AAS* **3**, 9 (2019).
21. Waniak, W., Zola, S. & Krzesiński, J. Dust emission for comets Shoemaker-Levy 1991a1 and McNaught-Russell 1993v. *Icarus* **136**, 280–297 (1998).
22. Boe, B. et al. The orbit and size-frequency distribution of long period comets observed by Pan-STARRS1. *Icarus* **333**, 252–272 (2019).
23. Snodgrass, C. et al. The size distribution of Jupiter family comet nuclei. *Mon. Not. R. Astron. Soc.* **414**, 458–469 (2011).
24. Drahus, M. Rotational disruption of comets with parabolic orbits. In *DPS Meet.* **46**, 200.04 (AAS, 2014).
25. Jewitt, D. Color systematics of comets and related bodies. *Astron. J.* **150**, 201 (2015).
26. Solontoi, M. et al. Ensemble properties of comets in the Sloan Digital Sky Survey. *Icarus* **218**, 571–584 (2012).
27. Jewitt, D. The active Centaurs. *Astron. J.* **137**, 4296–4312 (2009).
28. Fulle, M. in *Comets II* (eds Festou, M. et al.) 565–575 (Univ. Arizona Press, 2004).
29. Fulle, M., Mikuž, H. & Bosio, S. Dust environment of comet Hyakutake 1996B2. *Astron. Astrophys.* **324**, 1197–1205 (1997).
30. Jewitt, D. et al. Interstellar interloper 1I/2017 U1: observations from the NOT and WIYN telescopes. *Astrophys. J. Lett.* **850**, L36 (2017).
31. Do, A., Tucker, M. A. & Tonry, J. Interstellar interlopers: number density and origin of 'Oumuamua-like objects. *Astrophys. J. Lett.* **855**, L10 (2018).
32. Moro-Martín, A., Turner, E. L. & Loeb, A. Will the Large Synoptic Survey Telescope detect extra-solar planetesimals entering the Solar System? *Astrophys. J.* **704**, 733–742 (2009).
33. Marsden, B. G., Sekanina, Z. & Yeomans, D. K. Comets and nongravitational forces. V. *Astron. J.* **78**, 211–225 (1973).
34. Cowan, J. J. & A'Hearn, M. F. Vaporization of comet nuclei: light curves and life times. *Moon Planets* **21**, 155–171 (1979).
35. Jorda, L., Crovisier, J. & Green, D. W. E. The correlation between visual magnitudes and water production rates. In *Asteroids, Comets, Meteors 2008* **1405**, 8046 (LPI, 2008).
36. Rodgers, C. T. et al. Improved u'g'r'i'z' to UBVRcIc transformation equations for main-sequence stars. *Astron. J.* **132**, 989–993 (2006).
37. A'Hearn, M. F. et al. Comet Bowell 1980b. *Astron. J.* **89**, 579–591 (1984).
38. Weiler, M. et al. The dust activity of comet C/1995 O1 (Hale-Bopp) between 3 AU and 13 AU from the Sun. *Astron. Astrophys.* **403**, 313–322 (2003).
39. Campins H. & Fernández Y. Observational constraints on surface characteristics of comet nuclei. *Earth Moon Planets* **89**, 117–134 (2002).
40. Sekanina, Z. in *Comets* (ed. Wilkening, L. L.) 251–287 (Univ. Arizona Press, 1982).
41. Samarasinha, N. H. et al. In *ESA Proc. 20th ESLAB Symposium on the Exploration of Halley's Comet* Vol. 1, ESA SP-250, 487–491 (ESA, 1986).
42. Jewitt, D. Cometary rotation: an overview. *Earth Moon Planets* **79**, 35–53 (1997).

NATURE ASTRONOMY   LETTERS

43. Drahus, M. & Waniak, W. Non-constant rotation period of comet C/2001 K5 (LINEAR). *Icarus* **185**, 544–557 (2006).
44. Davidsson, B. J. R. Tidal splitting and rotational breakup of solid biaxial ellipsoids. *Icarus* **149**, 375–383 (2001).
45. SDSS photometric equations. *SDSS* http://classic.sdss.org/dr7/algorithms/jeg_photometric_eq_dr1.html (2005).

Author contributions

K.R. and P.G. developed Interstellar Crusher. P.G. and M.D. designed the observations, wrote the telescope time proposal, performed photometry, estimated the size of the nucleus and wrote the paper. P.G. computed the orbit. M.D. compared the colour to Solar System comets and estimated the probability of rotational disruption. W.W. reduced raw images and performed Monte Carlo dust modelling. G.C. and I.P.-M. obtained data at the William Herschel Telescope.

Competing interests

The authors declare no competing interests.

Additional information

Supplementary information is available for this paper at https://doi.org/10.1038/s41550-019-0931-8.

Correspondence and requests for materials should be addressed to P.G. or M.D.

Reprints and permissions information is available at www.nature.com/reprints.

Publisher's note Springer Nature remains neutral with regard to jurisdictional claims in published maps and institutional affiliations.

Article

Gaseous atomic nickel in the coma of interstellar comet 2I/Borisov

Piotr Guzik[1] & Michał Drahus[1]

On 31 August 2019, an interstellar comet was discovered as it passed through the Solar System (2I/Borisov). On the basis of initial imaging observations, 2I/Borisov seemed to be similar to ordinary Solar System comets[1,2]—an unexpected characteristic given the multiple peculiarities of the only known previous interstellar visitor, 1I/'Oumuamua[3–6]. Spectroscopic investigations of 2I/Borisov identified the familiar cometary emissions from CN (refs. [7–9]), C_2 (ref. [10]), O I (ref. [11]), NH_2 (ref. [12]), OH (ref. [13]), HCN (ref. [14]) and CO (refs. [14,15]), revealing a composition similar to that of carbon monoxide-rich Solar System comets. At temperatures greater than 700 kelvin, comets also show metallic vapours that are produced by the sublimation of metal-rich dust grains[16]. Observation of gaseous metals had until very recently[17] been limited to bright sunskirting and sungrazing comets[18–20] and giant star-plunging exocomets[21]. Here we report spectroscopic observations of atomic nickel vapour in the cold coma of 2I/Borisov at a heliocentric distance of 2.322 astronomical units—equivalent to an equilibrium temperature of 180 kelvin. Nickel in 2I/Borisov seems to originate from a short-lived nickel-containing molecule with a lifetime of 340^{+260}_{-200} seconds at 1 astronomical unit and is produced at a rate of $0.9 \pm 0.3 \times 10^{22}$ atoms per second, or 0.002 per cent relative to OH and 0.3 per cent relative to CN. The detection of gas-phase nickel in the coma of 2I/Borisov is in line with the recent identification of this atom—as well as iron—in the cold comae of Solar System comets[17].

We observed 2I/Borisov with the X-shooter spectrograph of the Very Large Telescope at the European Southern Observatory (ESO) on 28, 30 and 31 January 2020 UT. At the time of the observations, the mean heliocentric and geocentric distances of the comet were 2.322 AU and 2.064 AU, respectively, and the mean heliocentric velocity was +19.16 km s^{-1}. X-shooter is a medium-spectral resolution instrument that simultaneously covers the spectral range between 3,000 Å and 2.5 μm, divided into three arms: near-ultraviolet and visible blue (UVB), visible, and near-infrared. However, for the present analysis we use only the UVB data. The UVB arm was configured to provide a spectral resolution of 4,100. The slit field of view was 1.3 × 10.88 arcsec, but the length was trimmed in the analysis to the inner 10.24 arcsec with low and uniform noise, corresponding to 1,950 × 15,300 km at the comet distance. For further details on the observations and data processing, see Methods.

A portion of the spectra presented in Fig. 1a, b show nine emission lines between 3,375 Å and 3,625 Å that are not associated with any species that are routinely or less frequently detected in Solar System comets. The two brightest lines are clearly visible in co-added spectra—both processed and unprocessed—from each night, and are invisible in equivalent spectra of the sky background; this effectively eliminates the possibility of confusion with a background source or instrumental artefacts.

Although the region between 3,375 Å and 3,625 Å does not overlap with the well known near-ultraviolet cometary emissions from OH, NH and CN (all three were also detected in our full spectrum from the UVB arm; see Extended Data Fig. 1), it does encompass the wavelengths of fainter emissions from OH, NH and CN, as well as H_2CO, S_2, and the cometary ions CO^+, CO_2^+, N_2^+ and OH^+, which have all been previously detected or sought in this spectral region in other comets[16,22–26]. However, we identified no combination of these species that would match the nine lines that we detected. Furthermore, from strong detections of OH at 309 nm, NH at 336 nm and CN at 387 nm, and from non-detections of CO^+ at 425 nm and 427 nm, CO_2^+ at 367 nm, and N_2^+ at 391 nm (all wavelengths correspond to the strongest bands of these species in our full spectrum), we conclude that these cometary species are undetectable in our data via the weaker emissions between 3,375 Å and 3,625 Å. We note that the detected nine lines are spatially compact (Fig. 1a) and spectrally unresolved (Fig. 1b), which renders their appearance distinct from that of the routinely observed compounds, such as OH, NH and CN.

We recognize the detected lines as the spectroscopic signatures of atomic nickel vapour, Ni I, which has previously been observed in the spectrum of sungrazing comet C/1965 S1 (Ikeya–Seki)[18,19]. To confirm the identity, we created a model of nickel fluorescence emission (see Methods), which is dependent on the heliocentric distance and heliocentric velocity of a comet (the former scaling the amount of incoming solar energy through the inverse-square law and the latter arising as a result of the Swings effect[27]). A model spectrum computed for the epoch of our observations is presented in Fig. 1c. The agreement with the observed spectrum of 2I/Borisov is very good, although minor differences exist and can be attributed to several factors. On the observation side, these factors include the observation noise, minor features in the baseline, and rather large spectral channels compared

[1]Astronomical Observatory, Jagiellonian University, Kraków, Poland. ✉e-mail: piotr.guzik@doctoral.uj.edu.pl; drahus@oa.uj.edu.pl
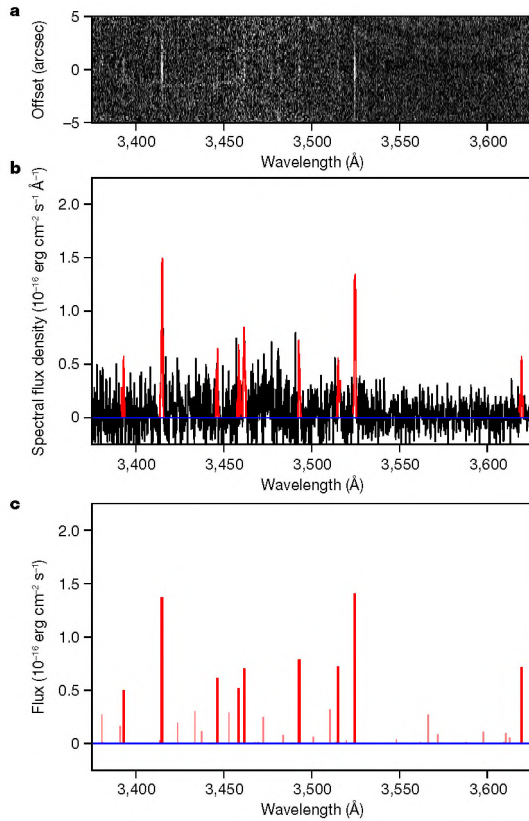
Article

Fig. 1 | Emission lines from gaseous atomic nickel in the near-UV spectrum of 2I/Borisov. a, Portion of the co-added and calibrated 2D spectrum with the dust-continuum component removed (see Methods). **b,** Corresponding 1D spectrum (see Methods) with the identified nickel emission lines highlighted in red. **c,** Modelled spectrum of nickel fluorescence emission (see Methods), converted to air wavelengths[28], and scaled to best match the two brightest lines.

to the line spread function (the last factor vanishing in the comparison of integrated line fluxes). The contributors on the model side are the limited accuracy of the input transition parameters, limited resolution,

coverage and accuracy of the solar spectrum used, and solar variability. Small differences are therefore not unexpected. The model predicts that no additional nickel lines will be detectable in other regions of the X-shooter spectrum (Extended Data Fig. 1). In Table 1 we show the measured fluxes of the detected nickel lines, their wavelengths and classifications, and the computed fluorescence efficiencies (see Methods).

The detected emission lines of nickel were further explored using the standard two-generation Haser model[29,30] (see Methods). First, we attempted to retrieve the parent and daughter scalelengths (see Methods) from the spatial profile of the lines along the slit, presented in Fig. 2. The sensitivity of spectral observations to these parameters is generally limited by the observation noise, and is further constrained by the spatial resolution (on the short side) and the extent of sampled coma region (on the long side). This restricts the usefulness of our data for such an analysis to the scalelengths (reduced to 1 AU from the Sun) ranging from about one hundred kilometres up to a few tens of thousands of kilometres. Figure 3a shows the results of the retrieval. It can be seen that the shorter scalelength reduced to 1 AU from the Sun is found at 170 km, corresponding to 920 km at the heliocentric distance of comet 2I/Borisov. This value is comparable to—but slightly greater than—the radial extent of the point spread function (PSF) in our data (see Methods), corresponding to 750 km at the geocentric distance of the comet. The short scalelength is therefore reliably constrained by the data. Conversely, the long scalelength is found at the upper limit of the investigated space, implying that only its lower bound might be constrained by the data. To determine the allowable regimes of the two scalelengths, we ran a Monte Carlo simulation (see Methods), the result of which is presented in Fig. 3b. Within one standard error, we found the shorter scalelength to be confined to a region between 70 km and 300 km, and the longer scalelength to be more than 18,000 km, both reduced to 1 AU. Assuming a constant gas expansion velocity[14] of 0.5 km s^{-1} and a negligible daughter excess speed, we found the corresponding lifetimes to be between 140 s and 600 s and more than 36,000 s, respectively (also at 1 AU). Although the Haser model alone does not enable us to distinguish which lifetime belongs to which generation, we can convincingly attribute the longer lifetime to nickel itself, consistent with its low photoionization rate[31] of 9.43 × 10^{-7} s^{-1}, equivalent to a lifetime of 1.06 × 10^6 s (both at 1 AU from the Sun).

Finally, using the Haser model with the constrained scalelengths and the assumed gas velocity, and using the model of nickel fluorescence emission, we obtained from the measured fluxes of the two brightest lines (see Table 1) a nickel production rate of 0.9 ± 0.3 × 10^{22} atoms per second (see Methods). Nickel is therefore a minor constituent of the coma of 2I/Borisov, with a relative abundance of 0.002% compared to OH and 0.3% compared to CN at the time of our observations (see Methods). The uncertainty of the production rate is estimated from

Table 1 | Measured, modelled and laboratory data for the detected nickel lines

Laboratory air wavelength (Å)	Measured flux (10^{-16} erg cm^{-2} s^{-1})	Modelled fluorescence efficiency at 1 AU[a] (10^{-13} erg s^{-1})	Upper level			Lower level		
			Configuration	Term	J	Configuration	Term	J
3,392.983	0.29 ± 0.12	0.6547	$3d^9(^2D)4p$	°	3	$3d^9(^2D)4s$	^3D	3
3,414.764	1.44 ± 0.13	1.7834	$3d^9(^2D)4p$	$^3F°$	4	$3d^9(^2D)4s$	^3D	3
3,446.259	0.48 ± 0.13	0.7963	$3d^9(^2D)4p$	$^3D°$	2	$3d^9(^2D)4s$	^3D	2
3,458.460	0.42 ± 0.15	0.6772	$3d^9(^2D)4p$	$^3F°$	2	$3d^9(^2D)4s$	^3D	1
3,461.652	0.88 ± 0.15	0.9196	$3d^8 (^3F)4s4p(^3P°)$	$^5F°$	4	$3d^9(^2D)4s$	^3D	3
3,492.956	0.56 ± 0.13	1.0223	$3d^9(^2D)4p$	$^3P°$	1	$3d^9(^2D)4s$	^3D	2
3,515.052	0.51 ± 0.11	0.9423	$3d^9(^2D)4p$	$^3F°$	3	$3d^9(^2D)4s$	^3D	2
3,524.536	1.34 ± 0.11	1.8276	$3d^9(^2D)4p$	$^3P°$	2	$3d^9(^2D)4s$	^3D	3
3,619.391	0.44 ± 0.07	0.9349	$3d^9(^2D)4p$	$^1F°$	3	$3d^9(^2D)4s$	^1D	2

[a]Calculated for the heliocentric distance and heliocentric velocity of 2I/Borisov and reduced to 1 AU from the Sun (see Methods).
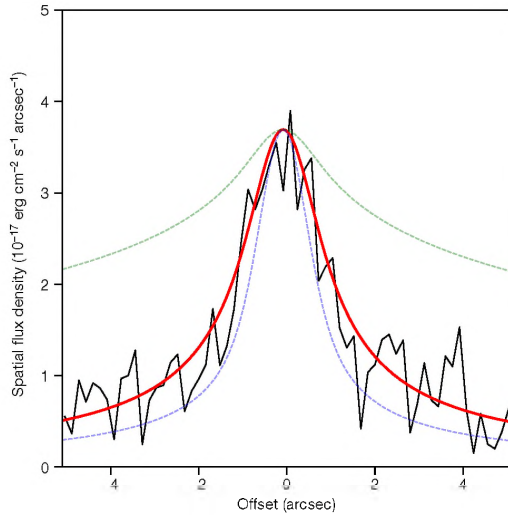J, total electronic angular-momentum quantum number.

Fig. 2 | Observed and modelled spatial profiles of nickel emission. The observed profile (black) is an average from the profiles of the two brightest lines. The modelled profile (red) was calculated using the standard two-generation Haser model with the best-matching combination of the parent and daughter scalelengths (see Methods). The standard deviation of the modelled profile from the observed profile is equal to 3.6×10^{-18} erg s^{-1} cm^{-2} arcsec^{-1}. For reference, also shown is a two-generation Haser profile calculated with the canonical CN scalelengths[32] (green) and a single-generation profile calculated with an infinite scalelength (blue). In the calculation of the modelled profiles we assumed the nominal extent of the PSF, equal to 1.0 arcsec (see Methods).
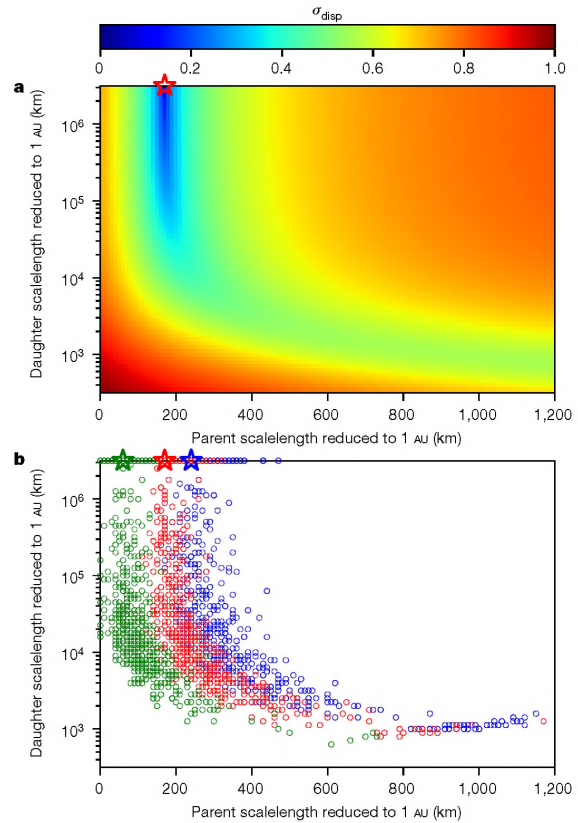

Fig. 3 | Haser scalelengths of the observed nickel emission. a, Map of the standard deviation of the model fits from the observed profile in Fig. 2, computed for the nominal extent of the PSF, equal to 1.0 arcsec (see Methods). The linear colour scale shows the quantity $\sigma_{disp} = ((\sigma - \sigma_{min})/(\sigma - \sigma_{max}))^\gamma$, where σ is the mapped standard deviation of the fit and $\gamma = 0.2$ was chosen empirically. **b,** Map of the solutions resulting from 3,000 Monte Carlo simulations, constructed from the observation noise for the minimum, nominal and maximum extents of the PSF, equal to 0.65 (blue), 1.0 (red) and 1.5 (green) arcsec, respectively (see Methods). The scatter within each PSF group shows the effect of the observation noise, whereas the spread of the groups illustrates the influence of atmospheric seeing. In both panels, the nominal solutions are indicated by the star symbols.

the errors of the measured line fluxes and correlated uncertainties of the PSF and parent and daughter scalelengths (propagated from the scatter in the Monte Carlo simulation), and it additionally accounts for an (assumed) 30% cumulative uncertainty of absolute flux calibration, fluorescence efficiencies and gas velocity. As can be seen in Extended Data Fig. 2, the variation of scalelengths and PSF within the allowable regimes has a small effect on the determined nickel production rate (see Methods).

Nickel is supplied in the Universe by exploding white dwarfs and exploding massive stars, with relative contributions of 71% and 29%, respectively[33]. Solid nickel is a major constituent of interplanetary matter, and is the second most abundant chemical element incorporated in iron meteorites in the form of FeNi alloys[34]. Measurements of metal ions in the upper atmosphere after meteor showers, obtained using a rocket-borne ion mass spectrometer, showed that the abundances of metal ions—including Ni—in meteors are compatible with the abundances in chondrite meteorites[35]. Very similar metal abundances were reported from the in situ analysis of dust around comet 1P/Halley[36]. FeNi alloys, as well as iron–nickel sulfides, were also present in all samples of cometary dust collected during the Stardust mission to comet 81P/Wild[37,38].

Although solid-phase nickel is widespread, observation of the gaseous form of nickel (and other metals) has been limited to hot environments. Notably, emissions from neutral nickel vapour and other gaseous metals were detected in comet C/1965 S1 (Ikeya–Seki) at heliocentric distances of approximately 30 and approximately 13 solar radii[18,19]. Several years later some faint, transient emission features that were attributed to nickel and silicon ions were observed in the solar corona shortly after the possible collision of comet C/1979 Q1 (Solwind) with the Sun[39]. More recently, an iron tail was indirectly identified in

comet C/2006 P1 (McNaught) at a heliocentric distance of less than 40 solar radii[20]. Gaseous metals were also detected in hot environments around other stars. They are observed in the atmospheres of ultrahot Jupiters[40,41] at equilibrium temperatures greater than 2,000 K, including a recent detection of atomic nickel vapour at WASP-121b[41]. Evaporation of numerous large exocomets is regarded as the most plausible explanation for the strongly variable metal absorption lines observed in the β Pic debris disk[21], with a measured Fe I gas temperature[21] of around 1,300 K. Disintegrating minor bodies are also thought to be the source of metal pollution in white dwarf atmospheres[42,43].

In this context, the detection of gaseous nickel at an interstellar comet travelling through the cold outskirts of the terrestrial planet region, at a distance of more than 2 AU from the Sun, is an unexpected finding. On the basis of observations of sungrazing and sunskirting comets, the equilibrium temperature needed for rocky dust to sublimate is greater than 700 K; this is high compared to the 180 K equilibrium

Article

temperature of 2I/Borisov at the time of our observations (see Methods). Even the subsolar equilibrium temperature of 260 K—which is consistent with the maximum nucleus temperature from realistic thermal modelling[44]—is much too low. In the absence of known non-solar high-temperature heat sources that are strong enough to cause dust sublimation at large heliocentric distances, and given the detected Haser scalelength of the nickel-containing parent, unbound nickel atoms seem to originate from the photodissociation of a short-lived nickel-containing molecule that sublimates at low temperatures or is otherwise released with major volatile compounds.

Until recently, atomic nickel has not been detected in the cold comae of Solar System comets. Notably, nickel was not detected by the Rosetta spacecraft at comet 67P/Churyumov–Gerasimenko in any form, and no heavy element was observed in the gas phase, despite the smaller heliocentric distance[45] of 1.5 AU. However, an independent study has shown that gaseous nickel (and iron) is indeed present in native Solar System comets up to large heliocentric distances, but has been overlooked in previous studies[17]. The simultaneous identification of this species in the cold comae of both 2I/Borisov and local comets shows that they have even more similarities than was previously thought, and strengthens the affinity between the unknown birthplace of 2I/Borisov and our own Solar System. However, whether analogues of Solar System minor bodies are widespread throughout the Galaxy is yet to be seen; although 2I/Borisov is markedly similar to Solar System comets, the only previous known interstellar visitor, 1I/'Oumuamua, was quite different[3-6]. New discoveries of interstellar minor bodies are expected at an increased rate after the commencement of the Vera C. Rubin Legacy Survey of Space and Time[46], which might help us to answer this question.

Online content

Any methods, additional references, Nature Research reporting summaries, source data, extended data, supplementary information, acknowledgements, peer review information; details of author contributions and competing interests; and statements of data and code availability are available at https://doi.org/10.1038/s41586-021-03485-4.

1. Guzik, P. et al. Initial characterization of interstellar comet 2I/Borisov. *Nat. Astron.* **4**, 53–57 (2020).
2. Jewitt, D. & Luu, J. Initial characterization of interstellar comet 2I/2019 Q4 (Borisov). *Astrophys. J. Lett.* **886**, 29 (2019).
3. Fraser, W. C. et al. The tumbling rotational state of 1I/'Oumuamua. *Nat. Astron.* **2**, 383–386 (2018).
4. Meech, K. J. et al. A brief visit from a red and extremely elongated interstellar asteroid. *Nature* **552**, 378–381 (2017).
5. Drahus, M. et al. Tumbling motion of 1I/'Oumuamua and its implications for the body's distant past. *Nat. Astron.* **2**, 407–412 (2018).
6. Micheli, M. et al. Non-gravitational acceleration in the trajectory of 1I/2017 U1 ('Oumuamua). *Nature* **559**, 223–226 (2018).
7. Fitzsimmons, A. et al. Detection of CN gas in interstellar object 2I/Borisov. *Astrophys. J.* **885**, L9 (2019).
8. De León, J. et al. Visible and near-infrared observations of interstellar comet 2I/Borisov with the 10.4-m GTC and the 3.6-m TNG telescopes. *Mon. Not. R. Astron. Soc.* **495**, 2053–2062 (2020).
9. Kareta, T. et al. Carbon chain depletion of 2I/Borisov. *Astrophys. J.* **889**, L38 (2020).
10. Lin, H. W. et al. Detection of diatomic carbon in 2I/Borisov. *Astrophys. J.* **889**, L30 (2020).
11. McKay, A. J., Cochran, A. L., Dello Russo, N. & DiSanti, M. A. Detection of a water tracer in interstellar comet 2I/Borisov. *Astrophys. J.* **889**, L10 (2020).
12. Bannister, M. T. et al. Interstellar comet 2I/Borisov as seen by MUSE: C2, NH2 and red CN detections. Preprint at https://arxiv.org/abs/2001.11605 (2020).
13. Jehin, E. et al. CBET 4719: COMET 2I/2019 Q4. http://www.cbat.eps.harvard.edu/cbet/004700/CBET004719.txt (2020).
14. Cordiner, M. A. et al. Unusually high CO abundance of the first active interstellar comet. *Nat. Astron.* **4**, 861–866 (2020).
15. Bodewits, D. et al. The carbon monoxide-rich interstellar comet 2I/Borisov. *Nat. Astron.* **4**, 867–871 (2020).
16. Feldman, P., Cochran, A. & Combi, M. in *Comets II* (eds Festou, M., Keller, H. U. & Weaver, H. A.) 425–447 (Univ. Arizona Press, 2004).
17. Manfroid, J., Hutsemékers, D. & Jehin, E. Iron and nickel atoms in cometary atmospheres even far from the Sun. *Nature* https://doi.org/10.1038/s41586-021-03435-0 (2021).
18. Preston, G. The spectrum of comet Ikeya-Seki (1965f). *Astrophys. J.* **147**, 718–742 (1967).
19. Slaughter, C. The emission spectrum of comet Ikeya-Seki 1965-f at perihelion passage. *Astron. J.* **74**, 929–943 (1969).
20. Fulle, M. et al. Discovery of the atomic iron tail of comet McNaught using the heliospheric imager on STEREO. *Astrophys. J.* **661**, L93 (2007).
21. Kiefer, F. et al. Fe I in the β Pictoris circumstellar gas disk. II. Time variations in the iron circumstellar gas. *Astron. Astrophys.* **621**, A58 (2019).
22. Kim, S. J., A'Hearn, M. F., Wellnitz, D. D., Meier, R. & Lee, Y. S. The rotational structure of the B–X system of sulfur dimers in the spectra of Comet Hyakutake (C/1996 B2). *Icarus* **166**, 157–166 (2003).
23. Valk, J. H. & O'Dell, C. R. Near-ultraviolet spectroscopy of comet Austin (1989c1). *Astrophys. J.* **388**, 621–632 (1992).
24. Cochran, A. L. A search for N2+ in spectra of comet C/2002 C1 (Ikeya-Zhang). *Astrophys. J.* **576**, L165–L168 (2002).
25. Cochran, A. L. & McKay, A. J. Strong CO+ and N2+ emission in comet C/2016 R2 (Pan-STARRS). *Astrophys. J. Lett.* **854**, L10 (2018).
26. Opitom, C. et al. High resolution optical spectroscopy of the N2-rich comet C/2016 R2 (PanSTARRS). *Astron. Astrophys.* **624**, A64 (2019).
27. Swings, P. Complex structure of cometary bands tentatively ascribed to the contour of the solar spectrum. *Lick Obs. Bull.* **19**, 131 (1941).
28. Peck, E. R. & Reeder, K. Dispersion of air. *J. Opt. Soc. Am.* **62**, 958–962 (1972).
29. Haser, L. Distribution d'intensité dans la tête d'une comète. *Bull. Acad. R. Sci. Liege* **43**, 740–750 (1957).
30. Combi, M. R., Harris, W. M. & Skyth, W. M. in *Comets II* (eds Festou, M., Keller, H. U. & Weaver, H. A.) 523–554 (Univ. Arizona Press, 2004).
31. Huebner, W. F. & Mukherjee, J. Photoionization and photodissociation rates in solar and blackbody radiation fields. *Planet. Space Sci.* **106**, 11–45 (2015).
32. A'Hearn, M. F., Millis, R. C., Schleicher, D. G., Osip, D. J. & Birch, P. V. The ensemble properties of comets: results from narrowband photometry of 85 comets, 1976–1992. *Icarus* **118**, 223–270 (1995).
33. Johnson, J. A. Populating the periodic table: nucleosynthesis of the elements. *Science* **363**, 474–478 (2019).
34. Wasson, J. T. *Meteorites* 11–38 (Springer, 1974).
35. Goldberg, R. A. & Aikin, A. C. Comet Encke: meteor metallic ion identification by mass spectrometer. *Science* **180**, 294–296 (1973).
36. Jessberger, E. K., Christoforidis, A. & Kissel, J. Aspects of the major element composition of Halley's dust. *Nature* **332**, 691–695 (1988).
37. Flynn, G. J. et al. Elemental compositions of comet 81P/Wild 2 samples collected by Stardust. *Science* **314**, 1731–1735 (2006).
38. Zolensky, M. E. et al. Mineralogy and petrology of comet 81P/Wild 2 nucleus samples. *Science* **314**, 1735–1739 (2006).
39. Chochol, D., Rušín, V., Kulčár, L. & Vanýsek, V. Emission features in the solar corona after the perihelion passage of Comet 1979 XI. *Astrophys. Space Sci.* **91**, 71–77 (1983).
40. Hoeijmakers, H. J. et al. Atomic iron and titanium in the atmosphere of the exoplanet KELT-9b. *Nature* **560**, 453–455 (2018).
41. Hoeijmakers, H. J. et al. Hot exoplanet atmospheres resolved with transit spectroscopy (HEARTS). *Astron. Astrophys.* **641**, A123 (2020).
42. Vanderburg, A. et al. A disintegrating minor planet transiting a white dwarf. *Nature* **526**, 546–549 (2015).
43. Xu, S. et al. The chemical composition of an extrasolar Kuiper-belt-object. *Astrophys. J. Lett.* **836**, L7 (2017).
44. Prialnik, D., Benkhoff, J. & Podolak, M. in *Comets II* (eds Festou, M., Keller, H. U. & Weaver, H. A.) 359–387 (Univ. Arizona Press, 2004).
45. Rubin, M. et al. Elemental and molecular abundances in comet 67P/Churyumov–Gerasimenko. *Mon. Not. R. Astron. Soc.* **489**, 594–607 (2019).
46. Ivezić, Ž., et al. LSST: from science drivers to reference design and anticipated data products. *Astrophys. J.* **873**, 111 (2019).

Methods

Additional details of the observations

As part of our custom calibration plan, we secured accurate absolute flux calibration by observing, on each night, spectrophotometric standard stars HD 111980 and HD 115169. The former was observed before the comet at a higher airmass and the latter after the comet at a lower airmass. Because of the extended nature of our target and the rather limited slit length, our nightly routine also included frequent integrations of the sky background at offset positions (10.0 arcmin on the first night and 5.0 arcmin on the following two nights). On the first night we took 400-s integrations and obtained 13 individual spectra of 2I/Borisov (O) and 6 spectra of the sky background (S) in the sequence OSOOSO, whereas on the second and third nights we took 240-s integrations, obtaining on each night 18 spectra of 2I/Borisov and 9 spectra of the sky background in the sequence OOS. All spectra were taken with the slit aligned with parallactic angle. Exposures of arc-lamps and flat-fields were also obtained as part of the X-shooter default calibration plan.

The target airmass was in the range 1.14–1.45 and the mean zenithal size of the seeing disk at 500 nm was equal to 0.76 arcsec in full width at half maximum (FWHM), extracted from the seeing measurements recorded at the start and end of the exposures. To determine the extent of the PSF applicable to our combined spectrum at the wavelengths of nickel emission, we scaled the recorded seeing values for airmass and wavelength using the canonical power laws with exponents of +0.6 and −0.2, respectively. The resulting effective seeing was equal to 0.92 arcsec, suggesting that the overall extent of the PSF (atmospheric and instrumental) was close to 1.0 arcsec, and was certainly within the range of 0.65 and 1.5 arcsec.

Data processing

All spectra were first processed using the ESO Reflex pipeline[47] to merge the orders, calibrate the wavelength (using arc-lamp spectra), correct for the flat-field (using flat-field integrations) and subtract inter-order background. We then cleaned the spectra of cosmic rays and other minor artefacts, filling them with the interpolated neighbourhood values.

Visual inspection of the individual integrations of 2I/Borisov showed four spectra in which the comet was out of the slit and five spectra in which the comet's signal was contaminated by background objects (cross-checked in Sloan Digital Sky Survey's images). These spectra were removed from further analysis. As an auxiliary procedure, the 2D spectra of the comet and sky background were summed along the spectral dimension to reveal faint background objects, which were then completely masked.

In each 2D sky spectrum, the signal along the spatial dimension was median-combined to produce a 1D version of the spectrum. Pairs of the 1D sky spectra bracketing integrations of the comet were then linearly interpolated to the middle time of the comet spectrum, and the result of this procedure was subtracted from every row of the comet's spectrum, effectively removing the sky-emission component. The resulting spectra were then flux-calibrated using observed and reference[54] spectra of two flux standard stars (see Methods section 'Additional details of the observations'). The reference spectra were recalculated to air wavelengths[28] and the observed spectra (natively in the air reference frame) were smoothed with a Gaussian kernel to match the spectral resolution and sampling of the reference spectra. This procedure enabled us to retrieve the extinction curve and instrumental response function for each night.

Repeating the previously described auxiliary procedure, we summed the sky-subtracted and flux-calibrated spectra of 2I/Borisov along the spectral dimension (wavelength range 3,600.0–5,400.0 Å) to find the brightness peak of the coma. This enabled us to vertically shift and average the individual 2D spectra. The resulting merged 2D spectrum had increased noise in the rows close to the edges of the spatial dimension; therefore, for the analysis we extracted the central part (64 pixels long; equivalent to 10.24 arcsec or 15,300 km at the comet). Subsequently, we summed this spectrum along the spatial dimension to create a 1D high signal-to-noise ratio wavelength-calibrated and flux-calibrated spectrum that was free of atmospheric emissions.

To remove the dust-continuum component, we selected two emission-free regions (4,390.0–4,500.0 Å and 5,200.0–5,320.0 Å) and least-square-fitted the spectrum of the Sun with an unrestricted linear spectral slope. For this procedure, we used a high-spectral-resolution solar irradiance atlas[48], which we recalculated to air wavelengths[28], Doppler-shifted to account for the heliocentic and geocentric velocities of the comet, and smoothed with a Gaussian kernel to match the spectral resolution and sampling of our data. The fit was then subtracted from the 1D spectrum of 2I/Borisov to produce the final spectrum that was used for the analysis.

Spectral line measurements

The line fluxes were consistently measured in 2-Å wavelength intervals (centred to a fraction of a spectral channel to maximize the recorded flux), and the noise was estimated from the nearest emission-free intervals to the left and right with a 5-Å width. The width of the flux interval was chosen as a compromise between the need to enclose the entire flux and cut out the unwanted noise. Thus, the actual signal-to-noise ratios of the detections might be higher.

Nickel fluorescence

To compute the fluorescence spectrum of nickel, we first solved statistical-equilibrium equations for 133 energy levels participating in 464 transitions listed in the Atomic Spectra Database of the National Institute of Standards and Technology (NIST)[49]. The equations balance the fluorescence absorption and emission, and can be written for each energy level i in the form:

$$\sum_{u>i} \phi_u R_{ui} + \sum_{l<i} \phi_l R_{li} = \phi_i \left(\sum_{u>i} R_{iu} + \sum_{l<i} R_{il} \right), \qquad (1)$$

where ϕ_i is the fractional population of the ith energy level, R_{lu} is the pumping rate between the lower level l and the upper level u, and R_{ul} is the decay rate between these levels. The pumping and decay rates are defined through the Einstein coefficients for spontaneous emission A_{ul}, prompt emission B_{ul}, and absorption B_{lu}:

$$R_{lu} = B_{lu} \mathcal{F}_\odot(\lambda) = A_{ul} \frac{w_u}{w_l} \frac{\lambda_{ul}^5}{8\pi hc^2} \mathcal{F}_\odot(\lambda), \qquad (2)$$

$$R_{ul} = A_{ul} + B_{ul} \mathcal{F}_\odot(\lambda) = A_{ul} \left(1 + \frac{\lambda_{ul}^5}{8\pi hc^2} \mathcal{F}_\odot(\lambda) \right), \qquad (3)$$

where $h = 6.62607015 \times 10^{-34}$ J s is the Planck constant, $c = 2.99792458 \times 10^8$ m s^{-1} is the speed of light, λ_{ul} is the transition wavelength, w_u and w_l are the statistical weights of the upper and lower energy levels, and $\mathcal{F}_\odot(\lambda)$ is the wavelength-dependent solar energy flux density (energy per unit time, unit surface area, and unit wavelength). $\mathcal{F}_\odot(\lambda)$ can be calculated from the solar irradiance spectrum (that is, energy flux density at 1 AU from the Sun) by scaling with the inverse square of heliocentric distance. Note that the right-hand sides of the last two equations were obtained by substituting the known relations between Einstein coefficients. The Einstein coefficient for spontaneous emission A_{ul} was taken from the NIST data. From the provided error flags we conclude that the errors of A_{ul} of the nine detected lines of nickel range between ≤18% and ≤25%. Moreover, in the computation of the absorption and prompt emission rates we used solar irradiance data from two sources: for the vacuum wavelength range 2,990.0–10,000.0 Å

Article

we used the high-resolution solar atlas[48] obtained with the spectral resolution of 500,000 and natively available in the vacuum reference frame (the same that we used for the dust continuum subtraction; see earlier in Methods); and for the range 2,000.6–2,990.0 Å we used 0.1-Å data[55], which we converted to vacuum wavelengths[28]. Outside the combined wavelength range of these two sources we assumed zero solar irradiance; this assumption affected only seven transitions and had a negligible effect on the result of the computation. The composite solar irradiance spectrum was then scaled by the inverse square of heliocentric distance, and Doppler-shifted in accordance with the comet's heliocentric velocity to account for the Swings effect[27]. The resulting set of equations is linearly dependent, but the dependence is removed after replacing one (any) of the equations with a normalization condition:

$$\sum_i \phi_i = 1. \tag{4}$$

The set was solved with the lower–upper (LU) decomposition method. As a result of this computation, we obtained fractional level populations ϕ_i for each of the 133 considered energy levels, and then obtained the fluorescence efficiencies g_{ul} for the 464 considered transitions using:

$$g_{ul} = \frac{hc}{\lambda_{ul}} \phi_u A_{ul}. \tag{5}$$

The fluorescence efficiency is conventionally reduced to 1 AU from the Sun, obtained by scaling with the inverse square of heliocentric distance.

The model was tested against the spectrum of comet C/1965 S1 (Ikeya–Seki) and provided an excellent fit to the spectrum taken at a heliocentric distance of approximately 30 solar radii[18]. A fit to the spectrum taken at around 13 solar radii[19], although still reasonable, is not as good, but is consistent with saturation effects of the photographic plate, and possibly affected by additional excitation and de-population mechanisms that operate at the boundary of the solar corona.

Haser model

The density distribution of neutral species in the cometary coma is conventionally described by the Haser model[29,30,50]. We used the standard two-generation version, in which isotropically ejected first-generation 'parent' species travel radially outwards and progressively decay, giving birth to second-generation 'daughter' species that continue along the same lines at the same speed, also progressively decaying. In this simple scenario, the number of daughter species dn_d contained in an infinitesimal volume dV is:

$$dn_d(r) = \frac{Q}{4\pi r^2 v} \frac{\rho_d}{\rho_p - \rho_d} (e^{-r/\rho_p} - e^{-r/\rho_d}) dV, \tag{6}$$

where r is the nucleocentric distance, Q and v are the production rate and speed of the species (the same for both generations in the assumed scenario), and ρ_p and ρ_d are the parent and daughter scalelengths; their corresponding lifetimes are $\tau = \rho/v$. For equal ρ_p and ρ_d the above equation becomes:

$$dn_d(r) = \frac{Q}{4\pi r^2 v} \frac{r}{\rho} (e^{-r/\rho}) dV, \tag{7}$$

where $\rho = \rho_p = \rho_d$ is the common scalelength. Integration of dn_d over infinite volume gives the total number of daughter species in the coma:

$$n_d = \frac{Q\rho_d}{v}. \tag{8}$$

Note that the shape of the daughter density distribution depends solely on the two scalelengths and can be conveniently traced through the fraction of daughter species contained in an infinitesimal volume dV:

$$df_d(r) = \frac{dn_d(r)}{n_d} = \frac{1}{4\pi r^2} \frac{1}{\rho_p - \rho_d} (e^{-r/\rho_p} - e^{-r/\rho_d}) dV, \tag{9}$$

which becomes:

$$df_d(r) = \frac{1}{4\pi r^2} \frac{r}{\rho^2} (e^{-r/\rho}) dV, \tag{10}$$

for equal ρ_p and ρ_d scalelengths. Integration of df_d over infinite volume obviously returns the normalization condition $f_d = 1$. It can be readily seen that the fraction of species df_d is invariant under the interchange of ρ_p and ρ_d, making it impossible to attribute the scalelengths to the generations on the basis of the shape of the density profile alone. The model becomes indefinite if both scalelengths are equal to zero; however, if only one scalelength is equal to zero, it becomes effectively reduced to the simpler single-generation version.

Although the Haser model ignores the additional isotropic velocity gained by the daughter species at creation, it can still produce realistic daughter density profiles and production rates, albeit with altered scalelengths and speed to compensate for the missing parameter[30,51]. Likewise, the implicated equality of the parent and daughter production rates is often poorly realized, as most parent species have multiple decay branches and most daughter species can be created via multiple avenues. However, the two production rates may still be calculated from one another if the parent–daughter photochemical path is well characterized in terms of the parent decay ratio and daughter origin ratio. In the calculation of nickel production rate we assumed that nickel originated from a single parent, but refrained from associating this production rate with the parent due to the unknown branching ratios of the parent.

The lifetime of the species changes with the square of heliocentric distance, and it is also dependent on the level of solar activity. It is normally given at a standard heliocentric distance of 1 AU to facilitate comparisons between species and comets. The scalelength changes in the same way if the species velocity is set constant. In this work we used the standard scaling with the square of heliocentric distance.

Haser scalelengths

To retrieve the two Haser scalelengths from our data, we generated a set of 9,801 synthetic Haser profiles along the slit length with different combinations of scalelengths and compared these profiles against the observed spatial profile (Fig. 2) in search of the best match. Each synthetic profile was calculated on a grid emulating the 1.3 × 10.24 arcsec (1,950 × 15,300 km) trimmed slit and consisting of 45 × 320 cells, oversampling the actual number of CCD pixels along the slit by a factor of 5. First, we integrated the fractions of the daughter species df_d along the line of sight using our in-house adaptive step-size integrator with error control. Next, the integrated fractions were convolved with the PSF approximated by a symmetric two-dimensional Gaussian with FWHM equal to 1.0 arcsec (see Methods section 'Additional details of the observations'). Finally, we binned the grid cells using a 45 × 5 bin size, which resulted in a one-dimensional synthetic profile along the slit sampled at 64 equally spaced points, consistent with the observed spatial profile. Note that the fractions df_d were consistently calculated with the comet nucleus offset from the slit centre by −0.083 arcsec (−0.52 pixels) along the slit length, consistent with the offset of the observed profile (determined from the best match of a single-generation infinite-lifetime density profile with an unrestricted offset along the slit). The entire set of synthetic profiles was based on

121 parent scalelengths equally spaced along a linear scale between 0 and 1,200 km, and 81 daughter scalelengths equally spaced along a logarithmic (base of 10) scale between $10^{2.5}$ and $10^{6.5}$ km, both at 1 AU from the Sun. Every profile from the set was individually scaled to best match the observed profile by minimizing the sum of squared residuals. As a result of this procedure, we could construct a map of standard deviation (Fig. 3a) and therein find the best solution.

Monte Carlo simulations

We used a Monte Carlo method to simulate the effect of the observation noise and seeing uncertainty on the determined Haser scalelengths and the production rate. The simulations were generated and analysed in three groups corresponding to the PSF FWHMs of 0.65, 1.0 and 1.5 arcsec, which we considered to be, respectively, the minimum, the nominal, and the maximum values applicable to our combined spectrum of nickel (see Methods section 'Additional details of the observations'). Each group consisted of 1,000 clones of the observed spatial profile along the slit length. The clones were generated from the best-matching synthetic Haser profile (with a group-specific PSF) by superimposing random realizations of noise. We assumed normally distributed noise with a constant standard deviation calculated as the root-mean-square deviation of the best-matching profile from the observed one. As with the original search for the Haser scalelengths, the clones from each group were linked with the best-matching combinations of scalelengths identified in a set of 9,801 synthetic Haser profiles with a compatible PSF, and used for the determination of a corresponding production rate. For details of the Haser profile computation see Methods section 'Haser scalelengths'.

Production rate

The production rate can be easily deduced from the observed emission. Assuming an optically thin regime, the measured energy flux F is simply the energy rate of a single emitter g_{ul}, known as the fluorescence efficiency or 'g-factor' (see Methods section 'Nickel fluorescence') multiplied by the number of emitters visible in the slit and divided by the area of a spherical surface at the distance of the observer Δ. Thus,

$$F = \frac{n^* g_{ul}}{4\pi\Delta^2}, \tag{11}$$

where $n^* = nf^*$, and the asterisk indicates that the quantities were calculated upon integration over the slit, to distinguish from the corresponding quantities calculated with infinite integration limits, introduced earlier in Methods section 'Haser model'. By further assuming the Haser density distribution and substituting equation (8), we obtain:

$$Q = \frac{4\pi\Delta^2 v}{\rho f^* g_{ul}} F. \tag{12}$$

Note that the last two equations hold for species of any generation.

Reference production rates of OH and CN

To facilitate a comparison of the production rate of nickel with that of common cometary species in 2I/Borisov, we calculated the production rates of OH and CN, which are both robustly detected in our data (see Extended Data Fig. 1). The flux of OH was measured to be $4.6 \pm 0.9 \times 10^{-15}\,\mathrm{erg\,s^{-1}\,cm^{-2}}$ (integrated between 3,070.0 Å and 3,110.0 Å) and the flux of CN was equal to $3.73 \pm 0.02 \times 10^{-15}\,\mathrm{erg\,s^{-1}\,cm^{-2}}$ (integrated between 3,850.0 Å and 3,885.0 Å). These fluxes imply OH and CN production rates of 3.6×10^{26} molecules per second and 2.5×10^{24} molecules per second, respectively, calculated using the standard two-generation Haser model (see Methods section 'Haser model') with the canonical parameters[32] and using the fluorescence efficiencies of $5.0 \times 10^{-15}\,\mathrm{erg\,s^{-1}}$

and $3.65 \times 10^{-13}\,\mathrm{erg\,s^{-1}}$, respectively, both applicable to our observing geometry[52,53]. Note that in this calculation we used a higher species' speed of 1 km s^{-1} (compared to 0.5 km s^{-1} used for nickel); this reflects the excess speed that OH and CN gain at creation (see Methods section 'Haser model'). The excess speed of nickel is unfortunately unknown, and as such it was neglected. A detailed study of these and other common species in the coma of 2I/Borisov, based on the X-shooter data, will be presented in a separate work.

Equilibrium temperature

The equilibrium temperature is the temperature that equilibrates the incoming and outgoing energy. The average equilibrium temperature T_{av} of a rotating spherical body orbiting the Sun is given by:

$$T_{av} = \left(\frac{L_\odot(1-A)}{16\pi\sigma R^2}\right)^{1/4}, \tag{13}$$

where $\sigma = 5.670374419 \times 10^{-8}\,\mathrm{W\,m^{-2}\,K^{-4}}$ is the Stefan–Boltzmann constant, $L_\odot = 3.828 \times 10^{26}$ W is the solar luminosity, A is the Bond albedo and R is the heliocentric distance. The maximum equilibrium temperature is reached at the subsolar point. In the extreme case of the rotation axis directed to the Sun (or a non-rotating body), the subsolar equilibrium temperature T_{ss} becomes:

$$T_{ss} = \sqrt{2}\,T_{av}. \tag{14}$$

In the calculation of the equilibrium temperatures of 2I/Borisov, we implicitly assumed a typical cometary albedo of $A = 0.04$. Note that the result is weakly dependent on the albedo as long as $A \ll 1$.

Data availability

The X-shooter raw data are available in the ESO archive at https://archive.eso.org. Source data are provided with this paper.

Code availability

The EsoReflex pipeline is available from the ESO website at https://www.eso.org/sci/software/esoreflex/. All custom codes are direct implementations of standard methods and techniques, described in detail in Methods.

47. Freudling, W. et al. Automated data reduction workflows for astronomy. The ESO Reflex environment. *Astron. Astrophys.* **559**, A96 (2013).
48. Kurucz, R. L. New atlases for solar flux, irradiance, central intensity, and limb intensity. *Mem. Soc. Astron. Ital.* **8**, 189 (2005).
49. Kramida, A., Ralchenko, Yu., Reader, J. & NIST ASD Team. *NIST Atomic Spectra Database (v.5.7.1)* (National Institute of Standards and Technology, accessed 22 October 2020); https://doi.org/10.18434/T4W30F.
50. Haser, L., Oset, S. & Bodewits, D. Intensity distribution in the heads of comets. *Planet. Sci. J.* **1**, 83 (2020).
51. Combi, M. R. & Delsemme, A. H. Neutral cometary atmospheres. I—An average random walk model for photodissociation in comets. *Astrophys. J.* **237**, 633–640 (1980).
52. Schleicher, D. G. & A'Hearn, M. F. The fluorescence of cometary OH. *Astrophys. J.* **331**, 1058–1077 (1988).
53. Schleicher, D. G. The fluorescence efficiencies of the CN violet bands in comets. *Astron. J.* **140**, 973–984 (2010).
54. Bohlin, R. C., Gordon, K. D. & Tremblay P.-E. Techniques and review of absolute flux calibration from the ultraviolet to the mid-infrared. *Publ. Astron. Soc. Pac.* **126**, 711 (2014).
55. Hall, L. A. & Anderson, G. P. High-resolution solar spectrum between 2000 and 3100 Å. *J. Geophys. Res.* **96**, 12927 (1991).

Article

Extended Data Fig. 1 | Complete spectrum of comet 2I/Borisov from X-shooter UVB arm. a, Flux-calibrated spectrum with fitted dust continuum (see Methods). **b,** Same as **a** but with the dust-continuum component removed. Major emission features are labelled. **c,** Modelled spectrum of nickel fluorescence emission (see Methods) scaled to best match the two brightest lines.

Article
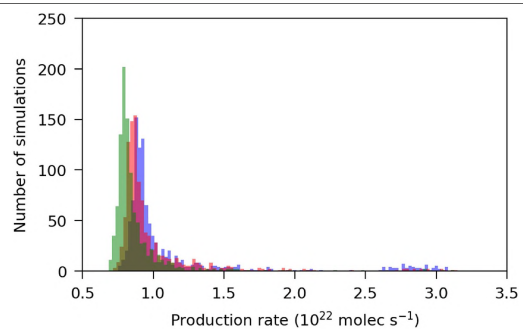
Extended Data Fig. 2 | Distribution of Monte Carlo-simulated production rates. The distribution was constructed from the production rates corresponding to the results of the Monte Carlo simulation in Fig. 3b (see Methods). Results are presented in three groups according to the assumed PSF equal to 0.65 (blue), 1.0 (red) and 1.5 (green) arcsec.